Moisture Sources in Laser Powder Bed Fusion Additive Manufacturing

Aniruddha Das

Department of Mining and Materials Engineering

McGill University, Montreal

March 2020

A thesis submitted to McGill University in partial fulfilment of the requirements of the degree of Master of Engineering

Abstract

Moisture can be responsible for oxygen uptake in laser powder bed fusion (LPBF) additive manufacturing (AM) processing. At high processing temperatures, the sensitive feedstock powders and parts can be affected by moisture-induced oxidation reactions. This work aims to evaluate the potential sources of moisture in LPBF AM processing and measure the quantity of moisture from each source. Two such major sources were investigated: (a) the filters used in additive manufacturing and (b) the surface of feedstock Ti-6Al-4V powders.

Using dynamic vapor sorption (DVS), the sorption properties of cellulosic fibre filters commonly used in LPBF AM were measured. It was shown that a significant amount of moisture can be stored within the filters during storage. The release of moisture from a non-treated filter was shown during LPBF processing. The sorption characteristics of Ti-6Al-4V feedstock powders were also determined using DVS and the surface of the powders was examined using X-ray photoelectron spectroscopy (XPS). Results show that the external titanium dioxide layer is minimally affected by atmospheric moisture during storage at room temperature.

The cellulosic filters used in the LPBF AM equipment were found to be a major source of moisture. Pre-drying was shown as an effective solution to the problem. The other moisture source i.e., surface adsorption on the metallic Ti-6Al-4V powders was found to be a minor concern.

Résumé

L'humidité peut être responsable de l'absorption d'oxygène lors du processus de fabrication additive (FA) par fusion sur lit de poudre au laser (FLPL). À des températures de traitement élevées, les réactions d'oxydation induites par l'humidité peuvent avoir une incidence sur les poudres et les composants. Ce travail vise à évaluer les sources potentielles d'humidité lors du processus de FA par FLPL et à mesurer la quantité d'humidité provenant de chaque source. Deux sources principales d'humidité ont été étudiées: (a) les filtres utilisés dans la fabrication additive et (b) la surface des poudres de Ti-6Al-4V.

En utilisant la gravimétrie d'adsorption de vapeur d'eau (DVS, en anglais), nous avons mesuré les propriétés de sorption des filtres à fibres cellulosiques couramment utilisés dans le processus de FA par FLPL. Il a été démontré qu'une quantité importante d'humidité peut être stockée dans les filtres pendant l'entreposage. La libération d'humidité à partir d'un filtre non traité a été mise en évidence lors du processus de FLPL. Les caractéristiques de sorption des poudres de Ti-6Al-4V ont également été déterminées par DVS et la surface des poudres a été examinée par spectrométrie photoélectronique X (XPS, en anglais). Les résultats montrent que la couche externe de dioxyde de titane est très peu affectée par l'humidité atmosphérique pendant l'entreposage à température ambiante.

Les filtres cellulosiques utilisés dans l'équipement de FA par FLPL se sont avérés être une source majeure d'humidité. Le pré-séchage est apparu comme une solution efficace au

problème. L'autre source d'humidité, à savoir l'adsorption en surface sur les poudres métalliques de Ti-6Al-4V, s'est révélée être une préoccupation mineure.

Acknowledgements

It has been an eventful journey at McGill and Montreal. I would like to thank Prof. Mathieu Brochu for his excellent supervision, support, clarity and guidance. He provided an immense number of opportunities and resources to think, share and collaborate our work at and beyond McGill.

A heartfelt thanks to the researchers I worked with, Eileen, Beto, Pierre and Amy, it wouldn't be possible without your help, dedication and guidance at every step. I am lucky to have worked with you. Additionally, I would like to thank Prof. Kristian Waters for permitting to utilize the mineral processing laboratory and all the of the Renishaw, Canada crew for your valuable discussions and material support.

Working at the Powder Processing and Additive Manufacturing (P^2AM^2) group was always a pleasure. I would remember the many conferences, activities and fests we celebrated together for such a large research group. I hope that spirit of teamwork still binds us in the future as a part of this happy family.

My heartiest applause for Barbara, June, Leslie, to all other staff and Professors from the Mining and Materials Engineering Department for your dedication. All your hard work integrates to keep the department active and running, day in day out.

Cheers to some amazing friends I made here: Amit, Pramod, Tuhin, Max, Tiffany, Sophia, Karan, Kirk, Kostas, Cristina, Oscar, An, Sara, Konstantina, Luis, Majid, Mauro, Jeff, and many more. A special thanks, to Andre for his sincere efforts to bring the department together. I wish him a great term as president of the departmental graduate student association (MMGESA) and captain of the soccer/foosball team. Furthermore, I was

fortunate to be volunteering for the MetSoc McGill Chapter and was associated with the McGill Outdoors Club; I wish them the very best in the days to come.

I am very grateful for the generous research support and training by the Natural Sciences and Engineering Research Council (NSERC) of Canada (NSERC Project Number: NETGP 494158 – 16) and Mitacs, Canada for awarding the Globalink Graduate fellowship.

Finally, I would dedicate this work to my family, without them anything wouldn't be possible so far.

Table of Contents

List of Figures

List of Tables

Chapter 1

Introduction

1.1. General introduction and motivation

Laser powder bed fusion (LPBF) is a popular additive manufacturing technique (AM) used to manufacture (or print) metallic [1.1,1.2], ceramic [1.2] and polymeric materials [1.2]. It uses one or more laser(s) to melt a specific track of powder which is referred as scanning [1.2,1.3]. For metallic materials, LPBF offers manufacturing of complicated and intricate shapes impossible to manufacture using conventional techniques [1.4]. One such example would be the printing of lattice structures which are aimed for weight saving applications [1.5,1.6]. **Figure 1.1.** (a) demonstrates the printing of thin struts and lightweight lattice structures. The 'spider bracket' shown in **Figure 1.1.** (b), jointly developed by Renishaw Plc and Altair is an example of an advanced design using lattice structures and topology optimization [1.7]. Parts like these are optimised to deliver adequate properties e.g. load-bearing while saving weight [1.6].

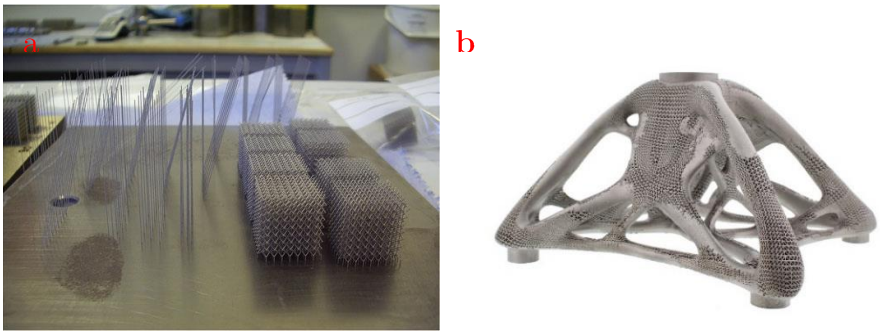

Figure 1.1. (a) Cubic lattice structures and thin single struts printed using LPBF AM [1.8] and (b) Demonstration of an advanced lattice optimised weight saving bracket known as the 'spider bracket' using Renishaw AM 250 [1.7].

LPBF also offers strict dimensional and compositional control. One of the major challenges in attaining perfect dimensional control is the build-up of residual stresses [1.9]. Compositional control is also required to maintain homogeneity and stay within specified compositional limits. Process parameter control is key towards achievement of dimensional accuracy and compositional homogeneity [1.10]. The challenges and complexities arise as there are over 60 optimizable processing parameters for LPBF AM [1.11].

Approved standards are required for printing/building parts while there is a shortage of material-specific standards [1.1,1.12]. There are several organizations e.g. ASTM, SAE, DICOM, etc. worldwide currently (in 2019) developing these standards. Along with appropriate standardization, desirable quality prints would require rigorous control of the overall processes constituting of,

- ensuring proper feedstock powder quality
- proper powder handling
- machine cleaning and maintenance
- process parameter control.

Adverse compositional changes in LPBF AM is possible due to the high temperatures (above melting temperature) typically generated in the process [1.13] and the reactive materials which are being printed (e.g. oxidizable materials such as Ti6Al4V). Amongst compositional changes, two adverse reactions are particularly important. First, adverse oxidation reactions from sources of oxygen [1.14,1.15] and second, the volatilisation of alloyants causing compositional inhomogeneity [1.16]. This work details on the source of oxidants, mainly moisture.

Moisture or water vapour is an oxidant for various metallic powders at elevated temperatures [1.17]. Unfortunately, the sources of moisture and their detailed impact for LPBF AM are lacking in the current literature. Moisture in LPBF AM can be responsible for detrimental effects including oxidation, surface micropores, and variation in part density [1.18,1.19]. This work investigates two sources of moisture with an attempt to quantify their contributions. A brief literature review (Chapter 2) has been provided describing an overview of LPBF operation, feedstock powders, recycling, compositional issues, and handling and sorption characteristics of selected materials. Chapter 3 describes the experimental methodology for the manuscripts presented in Chapter 4 and 5. Chapter 4 is a manuscript detailing moisture contribution from the filters commonly used in LPBF AM. Chapter 5 is another manuscript investigating the moisture adsorption characteristics of Ti6Al4V powder samples and details handling procedures. Finally, a detailed summary of the work has been presented in Chapter 6.

1.2. References

[1.1] Frazier, W. E. Metal Additive Manufacturing: A Review. *J. of Materi Eng and Perform* **23**, 1917–1928 (2014).

[1.2] Ngo, T. D., Kashani, A., Imbalzano, G., Nguyen, K. T. Q. & Hui, D. Additive manufacturing (3D printing): A review of materials, methods, applications and challenges. *Composites Part B: Engineering* **143**, 172–196 (2018).

[1.3] Bassoli, E., Sola, A., Celesti, M., Calcagnile, S. & Cavallini, C. Development of Laser-Based Powder Bed Fusion Process Parameters and Scanning Strategy for New Metal Alloy Grades: A Holistic Method Formulation. *Materials* **11**, 2356 (2018).

[1.4] Murr, L. E. *et al.* Metal Fabrication by Additive Manufacturing Using Laser and Electron Beam Melting Technologies. *Journal of Materials Science & Technology* **28**, 1–14 (2012).

[1.5] Rashed, M. G., Ashraf, M., Mines, R. A. W. & Hazell, P. J. Metallic microlattice materials: A current state of the art on manufacturing, mechanical properties and applications. *Materials & Design* **95**, 518–533 (2016).

[1.6] Du Plessis, A., Kouprianoff, D.-P., Yadroitsava, I. & Yadroitsev, I. Mechanical Properties and In Situ Deformation Imaging of Microlattices Manufactured by Laser Based Powder Bed Fusion. *Materials* **11**, 1663 (2018).

[1.7] Materialise. The Spider Bracket: A Topology Optimization Project by Altair, Materialise and Renishaw. Available at: https://www.materialise.com/en/cases/spider-bracket-a-topology-optimization-project-by-altair-materialise-and-renishaw. (Accessed: 2nd March 2020)

[1.8] Mines, R. Metallic Microlattice Structures: Manufacture, Materials and Application. *Springer International Publishing* (2019).

[1.9] Zaeh, M. F. & Branner, G. Investigations on residual stresses and deformations in selective laser melting. *Prod. Eng. Res. Devel.* **4**, 35–45 (2010).

[1.10] Letenneur, M., Kreitcberg, A. & Brailovski, V. Optimization of Laser Powder Bed Fusion Processing Using a Combination of Melt Pool Modeling and Design of Experiment Approaches: Density Control. *JMMP* **3**, 21 (2019).

[1.11] Brandt, M. (Ed.). Laser additive manufacturing: materials, design, technologies, and applications. *Woodhead Publishing* (2016).

[1.12] Pinkerton, A. J. (Invited) Lasers in additive manufacturing. *Optics & Laser Technology* **78**, 25–32 (2016).

[1.13] Lane, B., Moylan, S., Whitenton, E. P. & Ma, L. Thermographic measurements of the commercial laser powder bed fusion process at NIST. *Rapid Prototyping Journal* **22**, 778–787 (2016).

[1.14] Simonelli, M. *et al.* A Study on the Laser Spatter and the Oxidation Reactions During Selective Laser Melting of 316L Stainless Steel, Al-Si10-Mg, and Ti-6Al-4V. *Metall and Mat Trans A* **46**, 3842–3851 (2015).

[1.15] Scipioni Bertoli, U., Guss, G., Wu, S., Matthews, M. J. & Schoenung, J. M. In-situ characterization of laser-powder interaction and cooling rates through high-speed imaging of powder bed fusion additive manufacturing. *Materials & Design* **135**, 385–396 (2017).

[1.16] Zenou, M., & Grainger, L. (2018). Additive manufacturing of metallic materials. *Additive Manufacturing*. 53-103 (2018).

[1.17] Saunders, S. R. J., Monteiro, M. & Rizzo, F. The oxidation behaviour of metals and alloys at high temperatures in atmospheres containing water vapour: A review. *Progress in Materials Science* **53**, 775–837 (2008).

[1.18] Mukherjee, T., Zuback, J. S., De, A. & DebRoy, T. Printability of alloys for additive manufacturing. *Sci Rep* **6**, 19717 (2016).

[1.19] Li, X. P., O'Donnell, K. M. & Sercombe, T. B. Selective laser melting of Al-12Si alloy: Enhanced densification via powder drying. *Additive Manufacturing* **10**, 10–14 (2016).

Chapter 2

Literature Review

2.1. An overview of laser powder bed fusion

2.1.1. LPBF process for metallic materials

LPBF can be utilised to print metallic materials. To date, LPBF standards are available for the processing of a limited number of alloy systems including Ti6Al4V, SS316, In718, and few others. Many useful alloys and alloy systems such as several superalloys e.g. Hastelloy X [2.1], Rene 41 [2.2], CMSX-4 [2.3], rare earth-containing alloys such as Al-Mg-Sc-Zr [2.4], Yttrium modified Mg-Al-Zn [2.5], NdFeB [2.6], refractory materials such as tungsten alloys [2.7], CoCrMo refractory alloy [2.8], Ti-50Ta [2.9] to name a few are currently in development for LPBF AM.

A schematic of the chain of activities for an AM process is given in **Figure 2.1** Initially, a standard tessellation file (STL) is required [2.10], which is a surface representation of a 3D structure universally used for many AM processes including LPBF. Then this STL file is processed by a software which slices (provide the geometry for the individual layer) the 3D model, provides a position of the print on the build plate and considers the input parameters. This software generates a processed file which is the final input to the LPBF equipment.

Prior to running the print, the machine needs to be filled with powder. Most powder bed fusion machines use an overhead powder hopper for feeding powders into the system. A controlled amount of powder is deposited on the build plate as the print starts. After each laser scan, another dose of powder is deposited and subsequently spread by a recoater. The material, motion and the speed of recoating vary from equipment to equipment. Recoater or powder spreading is important as an uneven powder bed has correlated with higher porosities within the build [2.11]. This cycle of scanning and recoating continues until the build is finished.

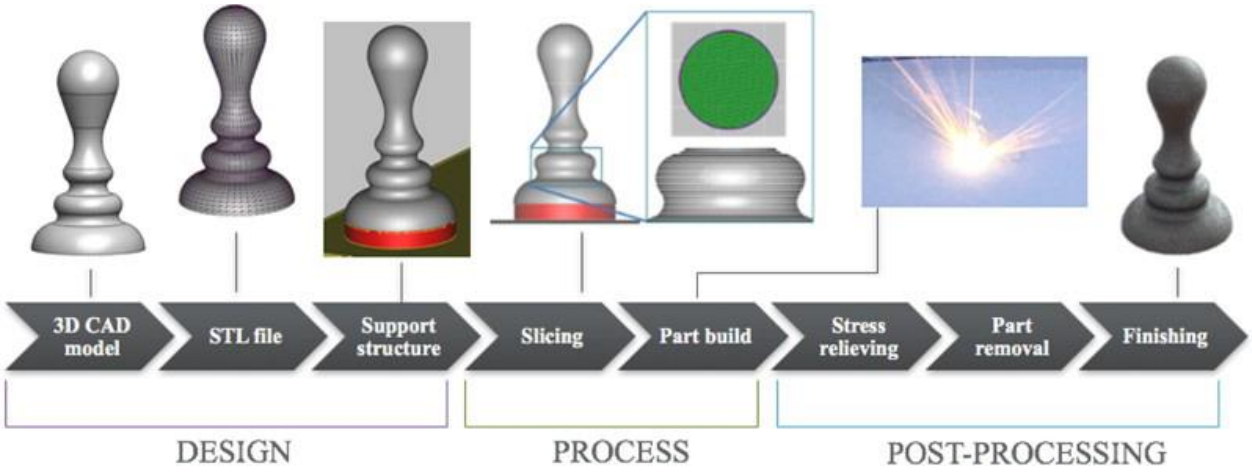

Figure 2.1. Design, processing and post-processing steps in LPBF AM (Adapted from Calignano et al. [2.12]).

After the print is completed, the unused powder is vacuumed from the build chamber of the machine. These powders are sieved and recycled for the next build. The build plate is cleaned and removed from the build chamber. Normally, the part along with the support structures are machined off the build plate using electrical discharge machining (EDM) or a band saw. The build plate is then given a rough polish and kept for reuse. Thereafter, the support structures conjoining the part is removed by machining.

Post-processing treatments including heat, chemical or surface treatment for the part might be necessary.

The cost of the metallic powders contributes to the maximum continuous expense in the life of LPBF equipment [2.13]. Therefore, powder recycling is essential in the life cycle of LPBF processing. Powder processing leads to the formation of large spatter particles [2.14] and agglomerates [2.14] which cannot be recycled. Therefore, the powders which are extracted from the system and intended for recycling are sieved to maintain proper size distribution [2.15]. Some LPBF equipment such as the Renishaw RenAM 500 Q [2.16], Concept Laser Xline 2000R [2.17] and EOS P 500 [2.18] do have the facility to recycle and reuse powders automatically. In that case, it reduces human handling of the powders. Few other steps are also necessary to maintain the LPBF equipment. These include mandatory change of the air filter which is commonly used to remove the small airborne particles generated during a print. The machine also requires to be thoroughly cleaned of previous powders if any powder of another material is scheduled to be printed next.

Ideally, the LPBF process is aimed to create full density parts requiring as fewer post-treatment steps as possible. Optimization of the input parameters, proper handling of the powder feedstock, correct usage and maintenance of the LPBF are key to obtaining desired results.

2.1.2. Production of powders for LPBF AM

The diameter of powders used for LPBF AM typically lies in the range of 25 to 45 µm which is smaller than the typical powder size range for electron beam melting (EBM) AM

(45 to 105 µm) [2.19]. LPBF alike many near net shape powder technologies e.g. Metal Injection Molding (MIM) and Hot Isostatic Pressing (HIP) require highly flowable powders [2.20]. Flowability has been defined as the 'ease of flow', it's a non-standardized factor dependent on the method of measurements such as the Hall/Carney flowmeters, dynamic angle of repose testing and others. Highly spherical powders exhibit high flowability [2.20] and maximize packing density [2.21]. Also, powders should be free from the surface or internal pores to avoid surface blistering in the printed part [2.22,2.23]. Chemically, the production process must be free from all adverse reactions, excessive segregations, and formation of unwanted phases.

Table 2.1 portrays a general overview of the major powder production processes along with their powder characteristics [2.24]. A few companies (AP&C, Pyrogenesis, Tekna in Canada, LPW in the UK, etc) in the world produce these powders.

Table 2.1. Major processes for manufacturing powder feedstock and their characteristics (Adapted and modified from Anderson et al. [2.24]).

Manufacturing process	Particle size (µm)	Advantages	Disadvantages	Common uses
Water atomization	0–500	• High throughput • Range of particle sizes • Only requires feedstock in an ingot form.	• Post-processing required to remove surface oxide • Irregular particle morphology • Satellites might be present • Wide particle size distribution (PSD) • Low yield of powder between 20–150 µm	Non-reactive powders
Gas atomization (Including electrode induction melting gas atomisation, EIGA)	0–500	• Wide range of alloys available • Suitable for reactive alloys. • Only requires feedstock in ingot form	• Presence of satellites • Wide PSD • Low yield of powder between 20–150 mm	Ni, Co, Fe, Ti (EIGA), Al
Plasma atomization	0–200	• Extremely spherical particles	• Requires feedstock to either be in wire form or powder • High-cost form	Ti (Ti64 most common)
Plasma rotating electrode process	0–100	• High purity powders • Highly spherical	• Low productivity • High cost •	Ti, Exotics
Centrifugal atomization	0–600	• Spherical particles • Satellites are generally not found • Substantial range of particle sizes (but difficult to get	• Difficult to make extremely fine powder unless very high speed can be achieved	Solder pastes, Zinc of alkaline batteries, Ti and steel shot

Apart from requirement needs, the produced feedstock powders for LPBF AM suffer from two major problems:

1. Formation of internal porosities: Presence of internal porosity is typical for gas atomized powders. **Figure 2.2** (a) shows the formation of such porosities. Alloy melt or semi-solid particles break up into droplets due to the gas flow. The fragments are stretched perpendicular to the direction of the gas to provide resistance to the incoming gas stream. As it solidifies, it spheroidizes to minimize surface tension but gas can remain trapped within as visible in **Figure 2.2** (b, c). Significant improvement has been made as the amount of porosity reported has been reduced in recent literature. Porosity values between 1-4 % have been reported by several researchers for various materials [2.24,2.25].

2. Agglomeration of powder particles: Powders with non-smooth surfaces and agglomerations are often formed using conventional techniques. **Figure 2.2** (b) shows such powders; the small particles sticking on the larger particles are commonly termed as "satellites". Satellite formation is commonly attributed to the faster solidification of fine droplets and collision with the already solidified larger powders during solidification [2.24]. Powder morphology varies from process to process e.g. plasma atomization produces lesser agglomeration than gas atomization.

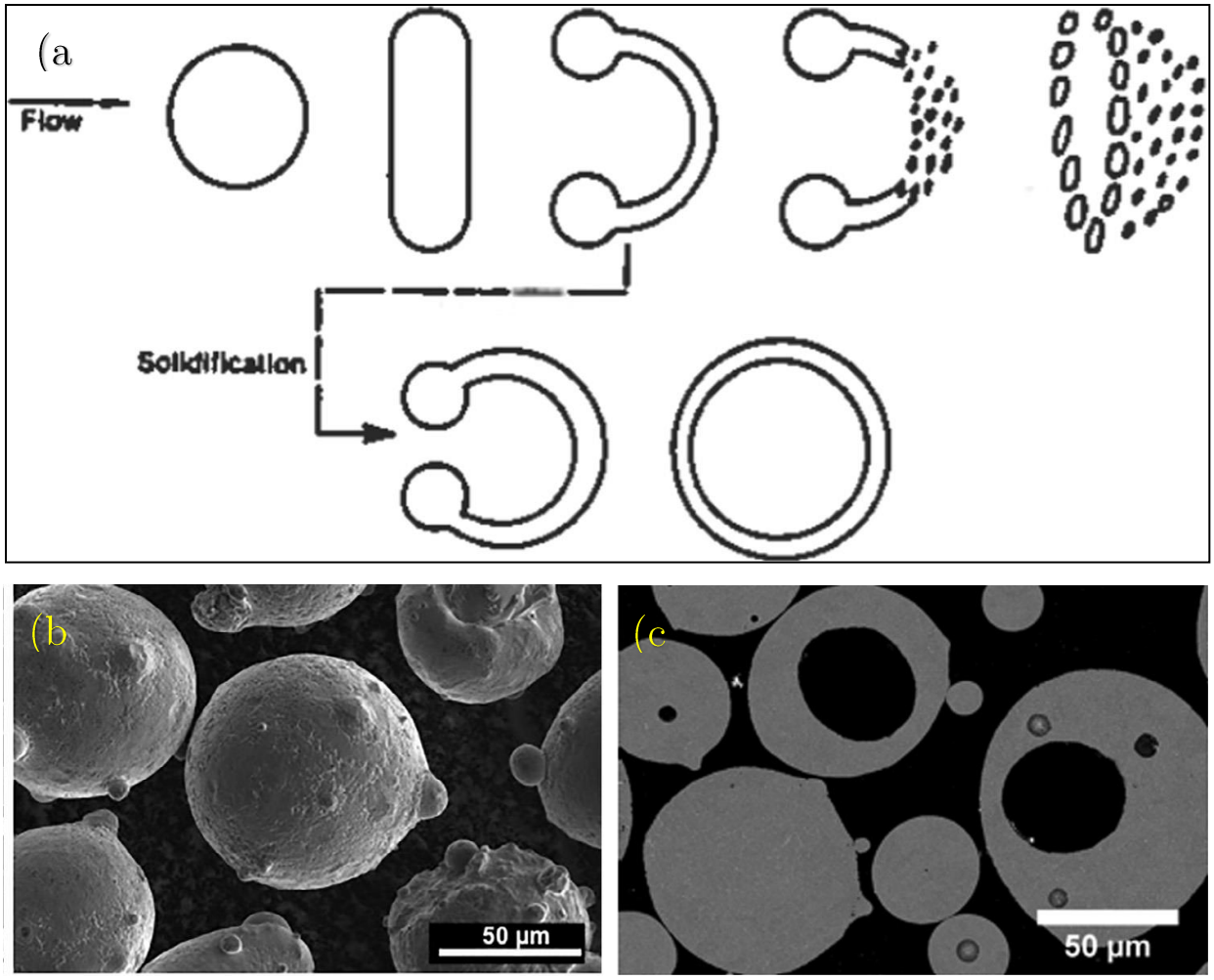

Figure 2.2. (a) Mechanism of formation of pores within gas atomised powders. SEM micrographs in backscattered imaging of (b) the exterior surface and (c) cross-section of the inert gas atomized MAR-M-247 powder in the size range of 45–106 micron (Adapted from Anderson et al. [2.24]).

Table 2.1 shows that a range of powder sizes are produced by conventional techniques. Within this range, only powders between a certain interval depending on the material (e.g. 15-45 µm for Ti, 20-53 µm for Al, etc.) are allowable for LPBF processing. Standardization of powder requirements or answer to the question 'What are the required powder properties to optimize the build?' is not yet available. Thus, provision of a 'perfect' feedstock requires research on the correlation of the powders and the built part.

The cost of these powders is very high compared to conventional non-powder feedstock. For example, LPBF AM grade Ti6Al4V powders can cost between 260 to 450 USD/kg and niobium powders can cost 1200 USD/kg [2.26]. This opens the door for research on relatively cheaper powder production technologies. One such example is an industrial attempt to produce AM grade Ti64 powders by plasma spheroidisation of cheaper feedstock [2.20,2.27]. Sun et al. [2.20] attempted spheroidisation utilizing a granulation sintering deoxygenation (GSD) process on cheap hydride-dehydride feedstock. Although the powder was not as spherical and had a higher oxygen content compared to the accepted processes, results for flowability and tap density (defined as the density after tapping a graduated cylinder until there is no volume change) were comparable to a similarly sized plasma atomised powder [2.20]. Additionally, mechanical means have also been used by some researchers to attain spheroidisation [2.28,2.29].

2.1.3. Powder property requirements for LPBF AM

As discussed previously, the desired powders inherent or intrinsic properties are high sphericity, required size range, minimal porosity, and compositional control. Some examples of important extrinsic or bulk properties are powder flowability, powder packing and presence of surface moisture. Firstly, the inherent properties can be correlated to some of the extrinsic properties such as Particle Size Distribution (PSD) and flowability. Secondly, all these properties are related to the properties of the printed parts. The correlation of characterized properties of powder with the printed parts suffer from gaps including lack of clear understanding and consensus [2.19]. In an LPBF system, proper powder flow and packing of the bed is vital. Absence of any of these would lead to build

failure. For this review, the views and data of three major physical powder characteristics: flowability, PSD and particle morphology are discussed.

LPBF AM requires powders with high flowability. Freely flowing powders are essential for proper powder flow during powder deposition through the hopper. For LPBF processes, a powder layer comprising few diameters of the particles must be spread by the recoater in a homogenous smooth fashion as shown in **Figure 2.3** (a). A proper smooth spread layer is free of any waviness (as in **Figure 2.3** (b)) and aggregates or clumps which ensures lesser and homogenous porosity in the built part [2.24].

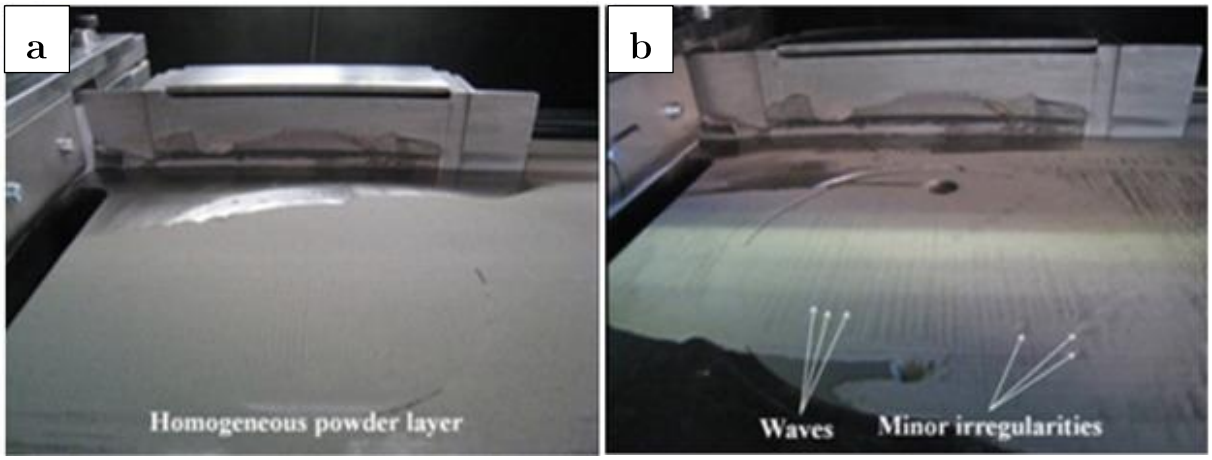

Figure 2.3. Depiction of powder spreading using a recoater in an LPBF build chamber (a) with a smooth spreading of a homogeneous powder layer and (b) with visible heterogeneous waviness and minor irregularities on the powder surface (Adapted from Yablokova et al.[2.31]).

Figure 2.4 gives a representation of the numerous intrinsic and extrinsic parameters involved in determining flowability. It can be observed that flowability is dependent on parameters such as wall friction, moisture content, surface tension, electrostatic interactions, and the orifice diameter. Thus, flowability is dependent on both the equipment which was used for its measurement (for example Hall or Carney

flowmeters) and the environment of its measurement (i.e. in inert gas, moist air or vacuum).

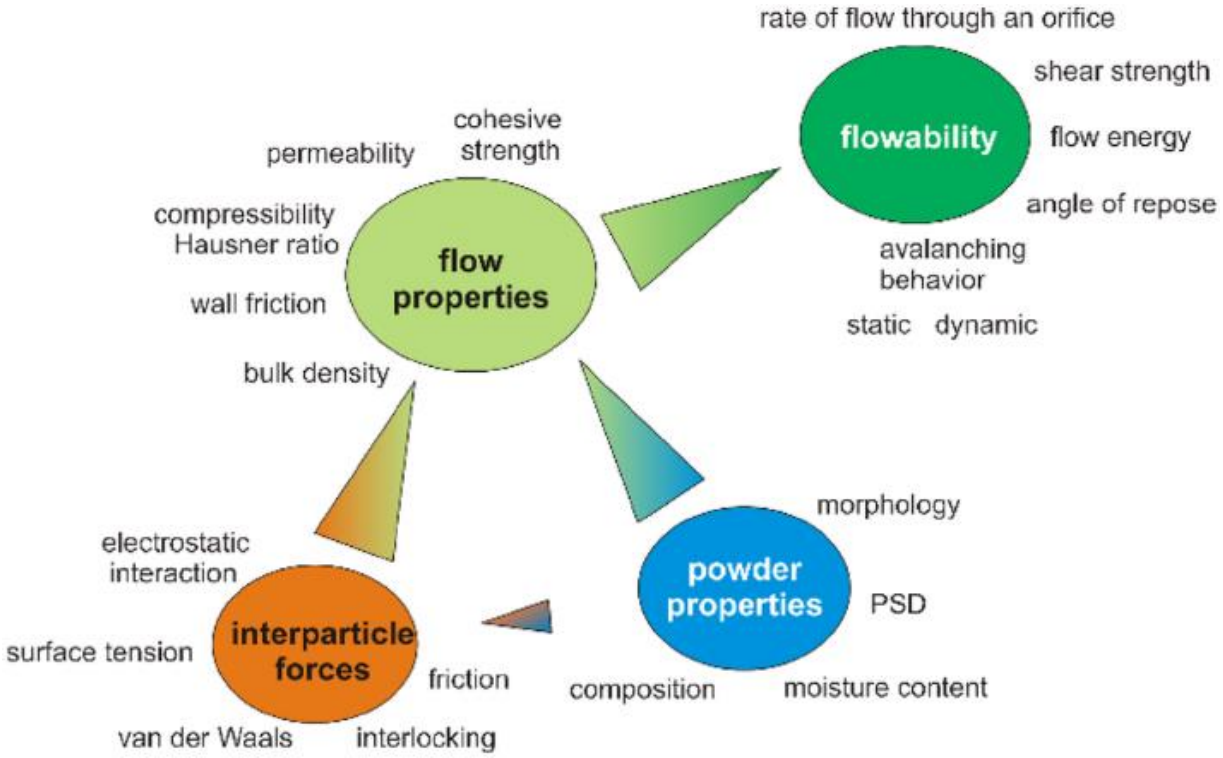

Figure 2.4. A visualization of the connection of flow-related parameters with the other influencing parameters (adapted and modified from Vock et al. [2.19]).

Flowability can be measured in various ways depending on the used instrument. Ideally, the method of determination of flowability should be close or replicate the physical process aimed to be measured, for example, flow through a hopper in LPBF AM. Thus, the best method to ascertain and compare flowability for LPBF would be to select a method which resembles powder flow in AM. Measurement of flowability by various researchers has been conducted using the Hall flowmeter, Carney flowmeter, Hausner ratio (ratio of tap and apparent density), angle of repose (AOR), shear testing and powder rheology measurements [2.19].

In order to be usable for LPBF AM, a flowability limit is often evaluated experimentally. **Figure 2.5** provides the result of a rotating drum (GranuDrum [2.32]) experiments for fine fractions of Ti, TiNbZn, NiTi and TiNb powder. In this case, the finer section of TiNb and TiNbZr (referred as TNZ-1 in **Figure 2.5**) powders are found to have a higher cohesive index (a measurand of cohesivity between powders [2.31,2.32]). Upon experiments, the TiNb powder was not found to be spreadable and the TNZ-1 powders had surface waviness upon spreading. In this case, despite the Hausner ratio criterion (ratio of tap and apparent density < 1.25) indicating excellent flowability for all the four powders, another testing method was necessary to identify issues with flowability [2.31].

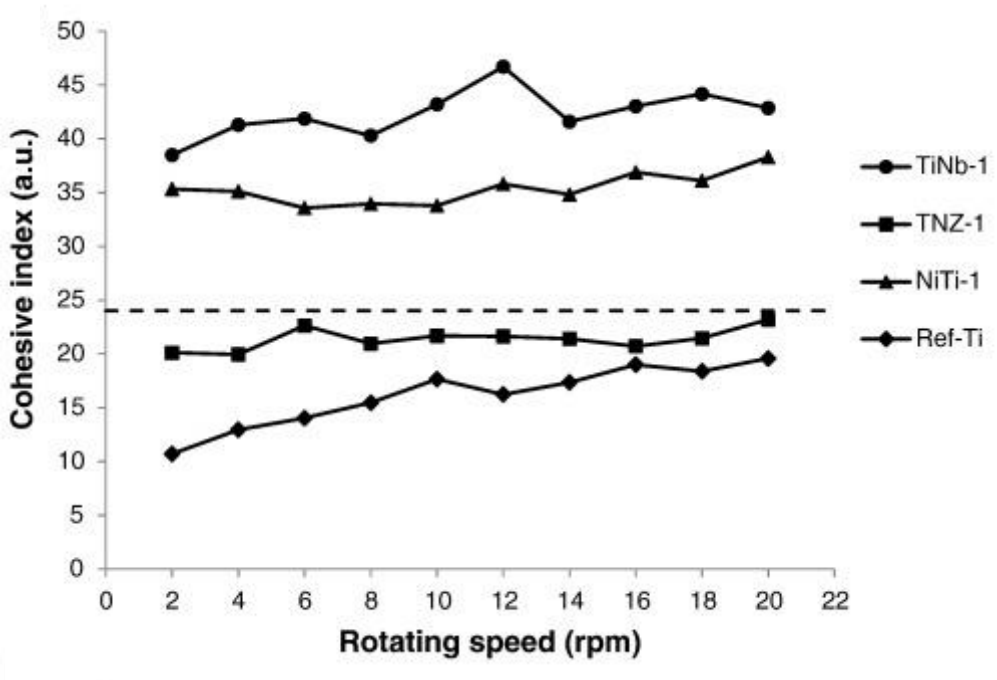

Figure 2.5. Cohesive index measurements using a rotating drum operating at various revolutions per minute for Ti, Ti-Nb-Zr (referred as TNZ-1 in the diagram), Ni-Ti and Ti-Nb powders (adapted from Yablokova et al. [2.31], the dotted line indicates the upper limit of cohesive index permissible for usage in LPBF AM).

Vock et al. [2.19] have conducted a detailed review of the current state of this topic. She concluded that each method has its merits and criticisms and a universal method is currently unavailable. Some general conclusions on flowability have also been stated by Vock et al. [2.19] ;

1. flowability generally increases with increasing powder sizes
2. flowability is enhanced by a narrower PSD
3. flowability is reduced in the presence of surface moisture.

Particle size distribution is the frequency distribution of powder sizes. There is definite evidence of the PSD to be one of the factors affecting bulk powder factors like powder flow and packing [2.19]. PSD affects the layer density of the recoated bed [2.33]. PSD has also been found to affect thermal conductivity which is an important parameter for this process [2.19]. Due to the presence of voids, a powder bed always has a lower conductivity than a solid bulk. Gong et al. [2.34] found the powder bed conductivity of a Ti6Al4V electron powder bed system to be half of the bulk. In another study on Ti6Al4V powders, smaller particles produced by rotating electrode (PREP) processes had higher powder bed conductivity than gas atomised powders [2.35].

Powder morphology also affects powder flowability and packing. In general, spherical particles with a smooth surface improve flowability. For a constant shape, finer particles generally are less flowable than coarser particles due to larger cohesive forces. Off spherical shapes during are prone to have mechanical interlocking which can lead to agglomerations or clumping resulting in the improper flow [2.24]. This, in turn, would

favour the development of porosity in the built parts. Presence of such porosity in built parts drastically reduces mechanical properties including fatigue resistance [2.24].

2.1.4. Correlation of powder and part properties in LPBF AM

Powder properties are responsible for the properties of the built part. Most of the papers focus on the relationship between changes in the PSD and the corresponding effects on the built part. There are also few papers relating the effects of bulk density and flowability on the built part. Apparent disagreements within the correlations exist. Powder properties which are translated to part properties may be material-specific due to differences in surface chemistry, physical parameters related to the bulk and the specifics of the experimental process.

Spierings et al [2.36] investigated 316L stainless steel with different PSDs. A wide PSD with more finer particles was suggested to improve densification [2.36]. The reason offered was finer particles melt faster than coarser particles leading to higher pore fill up [2.36]. In another study with gas-atomized 316L stainless steel by Badrossamay et al. [2.37], densification of powders with a coarser (-53/+20 µm, D_{50} = 42.5 µm) and finer (-20 µm, D_{50}= 16.6 µm) PSD was compared at various scan speeds keeping other parameters constant. Relatively lower densification was found that at higher scan speeds for the coarser set (-53/+20 µm, D_{50} = 42.5 µm) of powders. A similar phenomenon has also been observed for SS 316L by Liu et al. [2.38]. In all three cases, lowering of densification for coarser powders were attributed to the lower melt volume created at higher scan speeds for coarser powders compared to finer powders. A similar observation was noted for SS 304L by Abd-Elghany et al. [2.39] for various powder layer thicknesses in terms of

strength. A reduction in ductility was also noted in this case for higher layer thicknesses. Abd-Elghany et al. [2.39] inferred that the increase in coarse particles was also responsible for these effects. For SS 316L, Li et al. [2.40] found that gas atomised powders with a smaller average size (mean size 20 micron) had higher bulk densities compared to a water atomised powder (mean size 30 micron). The authors attribute both that it arises from both higher packing density of the smaller gas atomized powder and a larger quantity of oxygen in the water atomized powders. Although it has evidenced in the literature, only some aspects have been studied. An exact correlation between the powder and the part properties still require more experimentation and understanding.

2.1.5. Effects in powder handling and recycling.

Powder handling and reuse is an integral part of the LPBF process. According to a model, the maximum number use of a batch of powder varies around an average of 35 cycles, ranging from 1 to 117 cycles. Various losses reduce the powder use efficiency in LPBF AM. A study by Lutter-Gunther et al. [2.41] shows that the material efficiency (ratio of part weight to the weight of powder employed for the build) for 3 different materials were calculated to between 61.1 % and 63.5 %. This estimate of material efficiency is lower than previously calculated estimates of 79.6 % by Kellen et al. [2.42] and 91.6 % by Gebbe et al. [2.43]. Lutter-Gunther et al. [2.41] considered and evaluated an exhaustive list of recyclable and non-recyclable powder losses as defined in **Table 2.2**. Powder drains or wastes are uneconomic to be recycled [2.41]. Amongst these, the filter and the wet separator residue must be disposed of because the filter itself and the separator filtrate are disposed of. The aerosol emissions and surface adhesions are minor and unrecoverable.

Powders from the intermediate conditions are recyclable. Usually, these powders are recollected from the build chamber and overflow container and recycled.

Table 2.2. List of powder drains and intermediate conditions within LPBF process chain (Adapted from Lutter Gunther et al. [2.41])

	Powder Condition	**Description**
Powder Drains	Shield gas filter residue	Powder and spatter particles that have been carried away by shield gas stream and are collected in the filter.
	Wet separator residue	Powder and spatter particles that are collected in the wet separator filtering system.
	Aerosol emissions	Particles that are dispersed in the surrounding atmosphere as dust.
	Surface adhesions	Particles that adhere to surfaces (e. g. container walls, tools, machine walls, powder ducts).
	Part inclusions	Powder that is enclosed in inaccessible part regions (e. g. in support structures, which are often designed as hollow structures).
Intermediate Conditions	Storage Container	Unused powder that is stored in a suitable container for warehousing and transport.
	Machine Tank	Unused powder within the LPBF machine.
	Powder Bed	Non-solidified powder and spatter particles around the part or parts in the build volume.
	Overflow Container	Excessive powder from layer coating.

Variations in powder morphology have been observed with powder reuse. One such phenomenon is powder coarsening which has been observed for Ti6Al4V [2.15], IN 718 [2.44,2.45], 316L SS [2.46], 17-4PH SS [2.46] with recycling in LPBF AM. It's caused due to,

1. Sintering of powder particles which did not participate in the build (typically near the melt pool). **Figure. 2.6** (a, b, c) shows coarsening after 14 times reuse of IN718 powders. The virgin powders have noticeably lower agglomerate count. The shift towards higher powder sizes is apparent from the 7^{th} to the 14^{th} reuse.
2. Formation of larger spatter particles as shown in **Figure. 2.6** (d, e, f). Spatter is formed by the solidification of the ejected molten metal at the melt pool where the laser interacts with the powder [2.14,2.47]. Most spatter particles are spherical due to in-flight spheroidisation.

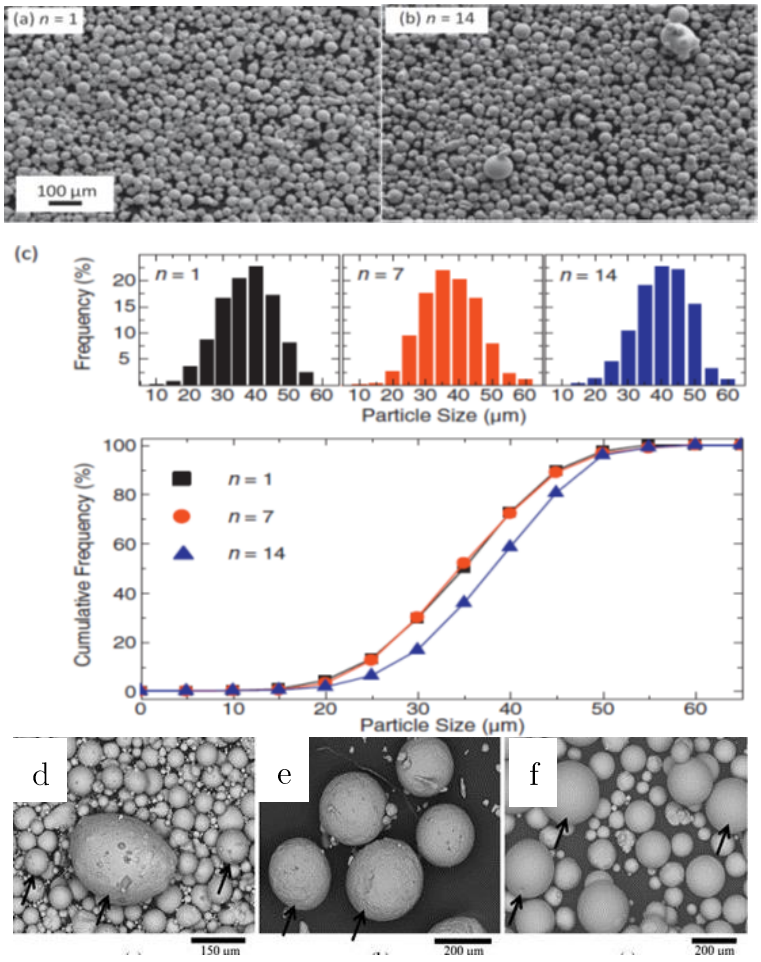

Figure 2.6. SEM image of IN 718 (a) Feedstock powder, (b) Powder after the 14th build, comparison of particle size distribution is shown in (c) in terms of relative (top) and cumulative (bottom) frequencies for the feedstock powders,7 and 14 times reused powders respectively. (adapted from Ardila et al. [2.45]) Spatter particles marked by arrows in (d) SS 316L, (e)Al-Si-10Mg and (f) Ti-6Al-4V feedstock powders (adapted from Simonelli et al. [2.14]).

Del Re et al. [2.48] conducted 8 cycles of powder reuse of with AlSi10Mg supplied by EOS. A small and gradual increase in the content of fine particles was observed. The origins of these fine particles were unexplained. This change in PSD might also be due to excessive powder coarsening of the larger powders which were sieved-out after the build. Kappes et al. [2.44] studied the powder recycling of IN718 (-45/+20) procured from

Concept Laser (Concept Laser, Germany). Elongated particles were found within the recycled IN 718 powders [2.44]. Presence of elongated particles has also been reported by Cordova et al. [2.49] for 38 powder reuse cycles (with topping up with an unspecified fraction of virgin powders) with IN 718 powders. The elongated particles resemble conjoined sintered particles, but the exact cause of this morphology change was not provided. Additionally, Kappes et al. [2.44] observed a lot of fine particles were generated upon reuse. Kappes et al. [2.44] suspected that these fines were generated from the cast-off powders in the build process or from mechanical attrition of the satellites during powder handling [2.44]. However, it was not investigated whether the fine particles were spatter or not. Moreover, satellite particles being sintered to the parent powders might not disjoin during powder handling.

Powder composition has been noticed to change in some powder recycling studies. In a study by Grainger [2.15] consisting of 38 continual reuse cycles with Ti6Al4V, a gradual gain of oxygen and nitrogen content of the powder was observed with increasing reuse cycles [2.15]. It was hypothesized that this arose from the hot powders near the melt pool which can react with the trace impurity gases within the chamber. For AlSi10Mg, Del Re et al. and Maamoun et al. [2.48,2.50] found no change in composition with 8 and 18 reuse cycles respectively. Using XPS analysis, even the surface composition of the reused powders was found to be unaffected [2.50]. Contradictorily, oxidation of 0.1 % was found for 6 continual reuse cycles of AlSi10Mg in a study by Cordova et al. [2.49]. It must be noted that the powder sizes, powder supplier, equipment and print parameters were different for these studies on AlSi10Mg. Thus, the results might not be exactly comparable. Ardila et al. [2.45] observed slight surface oxidation by EDS images for IN 718 after reusing the powder 14 times. It was concluded that the IN 718 powder is not susceptible to overall oxidation [2.45]. For powder reuse of 316L stainless steel, Leicht

[2.51] found an iron oxide layer on the powder surface along with oxide particles of Cr-Mn. In LPBF AM, Leicht [2.51] observed a lesser amount of these oxides than EBM AM. Two other works on stainless steel powders [2.52,2.53], however, do not report adverse compositional issues with recycling. Further compositional issues and mechanisms of adverse reactions are discussed in detail in section 2.2, compositional issues in LPBF.

Some data are available on the effect of reuse on the mechanical properties of the produced parts. Grainger et al. [2.15] found an increase in the ultimate tensile strength (UTS) and a decline in the elongation for Ti6Al4V powders with reuse. This was attributed to the rising oxygen content within the powders. O'Leary et al. [2.54] noted the oxygen content of a built part after single Ti6Al4V powder reuse to be higher than the grade 5 limit. Here the part is rendered useless as it has exceeded standard specification limits. A detailed explanation regarding the adverse oxidation reaction was not provided. Del Re et al. [2.48] found parts built using 8 times recycled AlSi10Mg powders to have a slight decline in tensile strength and high cycle fatigue (HCF) strength. There was no change in the composition and particle shape. The exact cause of these changes was not explained. Since the changes were small with 8 complete reuse cycles, powder reuse with topping up was concluded to be viable. LPBF powder reuse of stainless steels in three studies [2.51–53] showed no detrimental effects on the mechanical properties of the produced part. **Table 2.3** summarises the effect of powder reuse on the powder and part properties compiled from the literature on Ti6Al4V, AlSi10Mg, IN 718, SS 316L and SS 17-4 PH LPBF AM powders.

Table 2.3. Effect on powder and part properties with powder recycling in LPBF (adapted and modified from Vock et al. [2.19]).

Powder Material	**Maximum Number of Reuse**	**Effects on powder properties**	**Effects on part properties**	**Reference**
Ti6Al4V	12	Powder coarsening (shifting PSD) Flowability improves Apparent density increases	Density Increases Surface roughness increases Hardness: Slight increase UTS increases	Seyda et al. [2.55]
Ti6Al4V	38	Oxygen and Nitrogen content increases PSD: Slightly narrower, slightly coarser Flowability (Hall) increase Morphology: Constant	UTS: Slight increase	Grainger [2.15]
Ti6Al4V	5	PSD: Slightly coarser Morphology: Roughened surface Chemical composition: Constant O and N content	Chemical composition: Increased O-content	O'Leary et al. [2.54]
AlSi10Mg	18	PSD: Slightly finer Morphology: Slightly elongated Chemical composition: Constant	No effects	Maamoun et al. [2.50]
AlSi10Mg	8	Chemical composition: Constant PSD: slightly finer Tap and apparent density: Slight increase Morphology: Constant	UTS: decrease Yield strength: decrease HCF: decrease Surface roughness: constant	Del Re et al. [2.48]
AlSi10Mg	4	PSD: Constant Flowability (FT4): Constant		Vock et al. [2.56]
IN 718	14	Morphology: Constant PSD: constant, except agglomerates Chemical composition: constant	Microstructure: constant Porosity: constant Mechanical properties: constant	Ardila et al. [2.45]

IN 718	2	PSD: Significant increase in fines Morphology: Recycled powder more ellipsoidal, more oblique particles	Porosity/pore diameter/ pore spacing: weak correlation between the two powder conditions	Kappes et al. [2.44]
SS 316L	N.A.	Surface chemistry: the growing of Cr–Mn-rich oxide particulates		Leicht [2.51]
SS 316L	5		UTS: constant	Geisert et al. [2.52]
SS 17-4 PH	11	PSD: constant, slight shift to fines Flowability (Hall): increase Apparent density: increased Chemical composition: Constant Microstructure: BCC phase increased Morphology: Constant	Surface roughness: constant Density: constant Hardness: constant Mechanical properties: constant	Jacob et al. [2.53]
SS 17-4 PH	4	Morphology: Agglomeration PSD: Shift towards coarse		Barnhart [2.46]

2.2. Compositional issues in LPBF AM

LPBF involves high temperatures often above 2000 °C [2.57] and metallic powders that can be reactive in these conditions. Thus, for the metal powders, a probability of compositional change due to new phase formations, reactions, evaporation or dissolutions of atmospheric gases exists during LPBF processing. Additionally, evaporation or

volatilisation of alloyants having lower vapour pressure can occur at these high temperatures.

2.2.1. Oxidation and other adverse reactions

To prevent a reaction with oxygen or other atmospheric gases most LPBF units print in an inert gas atmosphere. This is achieved by using inert gases (commonly nitrogen or argon) to purge the system of atmospheric air and print in a stream of continuously flowing inert gas. In some LPBF equipment, a rough vacuum (Pressure > 0.1 Pa) is also used initially to accelerate the process of removing atmospheric air from the build chamber. After the evacuation, the inert gas is injected, it may be continually purged (with refilling) or be recirculated depending on the equipment. **Table 2.4** lists chamber atmosphere preparation strategies employed by some common LPBF equipment. The chamber atmosphere preparation is completed when an operator programmable 'Oxygen level' (generally in between 0-1000 ppm) is read by an oxygen sensor within the build chamber of the machine.

Table 2.4. Chamber atmospheric preparation method of some LPBF machines.

Manufacturer	Model Name	Has Argon Recirculation	Has Initial Evacuation
Concept Laser	M2 Cusing (2014)	No	No
SLM	125	Yes	No
EOS	M290	Yes	No
Renishaw	AM 250	Yes	Yes

Despite these measures, oxidation reactions have been commonly observed in LPBF AM [2.14]. Previously in Section 2.1.5, oxidation of powders and parts of reactive alloys like Ti6Al4V and AlSi10Mg has been detailed. The part might exceed specifications if the composition exceeds a certain standard limit e.g. Grade 5 or Grade 23 for Ti6Al4V powders. For Ti6Al4V, increasing oxygen content is detrimental as embrittlement occurs increasing tensile strength at the expense of ductility, fatigue strength and stress corrosion resistance. Apart from oxygen, gain in the nitrogen content has been observed for Ti6Al4V [2.15]. Similar to other interstitial elements for titanium, nitrogen also embrittles the alloy [2.58]. Bauer et al. [2.59] conducted a study with external atmosphere control with AlSi10Mg powders. Reduction of the total contaminant (oxygen and moisture) amount below 30 ppm minimized porosity and oxidation compared to tests conducted at 500 and >1000 ppm of contaminants. There are also other alloys where oxidation can be a major problem. The transformation temperature for shape memory alloys (e.g. NiTi) is affected by oxide contamination [2.60]. Hence the 'temperature' designed shape memory or superelastic alloys for LPBF can be affected by adverse oxidation.

2.2.2. Potential mechanisms of oxidation

In the current literature, an understanding of the sources of oxidants in the LPBF AM process is unavailable. No paper has detailed an exact model or source quantification for these reactions. Moreover, as already noted in Section 2.2.1, there is disparity and disagreement about the oxidant. Hypothetically, for metallic powders there can be two potential mechanisms of oxygen gain:

1. Reaction (or dissolution) of oxygen with the powders present in the build chamber.

2. Reaction of the powders with water vapour (moisture).

At high temperatures, gaseous oxygen has been found to react with various metals. **Figure 2.6** (a) shows the Ellingham diagram which is used to describe the free energies of formation at various partial oxygen pressures and temperature of oxidation. The metals placed in the lower section of the Ellingham diagram have lower free energy for metal oxidation reactions. Apart from reacting with oxygen gas, some metals also dissolve oxygen in significant quantities. Group IV A metals such as titanium, hafnium, zirconium have 30,28 and 20 % solubility of oxygen respectively in their low-temperature HCP (α) phase. Amongst all metals in the periodic table, titanium has the largest solubility of oxygen which can be observed in the large α Ti zone in the phase diagram of Ti-O (**Figure 2.6** (b)).

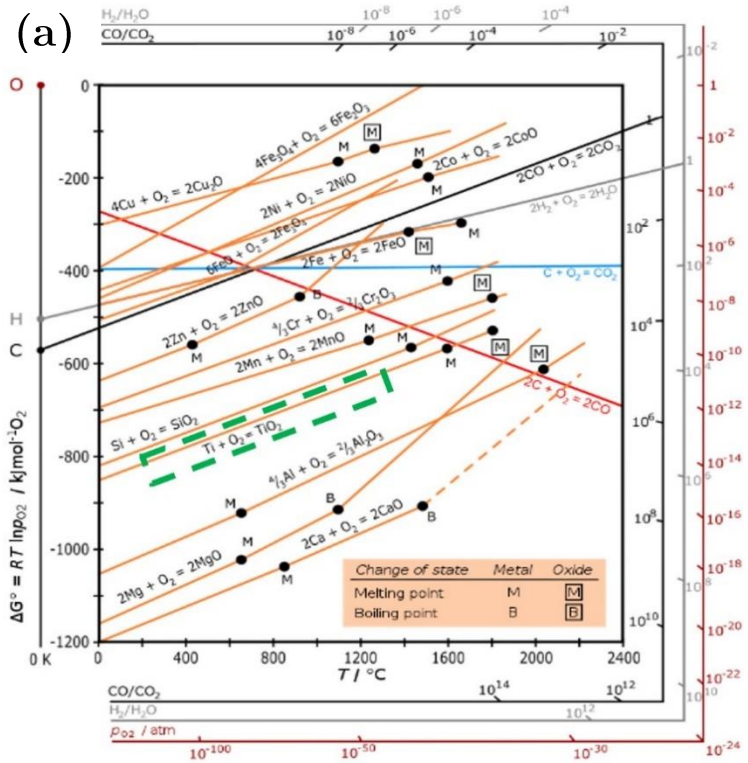

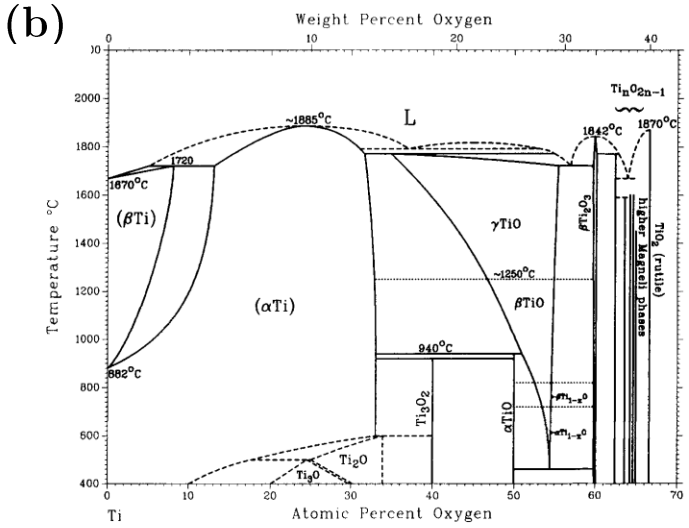

Figure 2.6. (a) Ellingham diagram depicting free energies of oxidation of various metals with temperature and partial pressure of oxygen [2.61]. The oxidation reaction of titanium has been highlighted by the green dotted box and (b) The Titanium-Oxygen phase diagram (adapted from Murray et al. [2.62])

Water vapour can also oxidize metals at high temperatures. Wouters et al. [2.63] provide a review of the thermal oxidation of titanium at elevated temperatures. **Figure 2.7** shows a comparison between the mass increase with time due to of oxidation of titanium at 20 mbar pressures of oxygen versus water vapour. For water vapour, the rate law describing oxidation is initially linear which gradually transitions into a parabolic rate law. The initial reaction is a rapid reaction at the surface by the H_2O molecules to form a consistent compact layer of TiO_2. A small film of this TiO_2 is formed, thereafter H_2O dissociates on the surface to form H^+ and OH^- ions. The OH^- diffuses inwards to the interface to oxidise Ti to TiO_2. Thus, the latter part of the reaction is parabolic (see **Figure 2.7**) and dependent on the rate of diffusion of the OH^- ions. In case of oxidation by oxygen, the initial TiO_2 formed is highly stratified compared to the compact TiO_2 formed due to oxidation by moisture. Additionally, OH^- ions (radius = 95 pm) being

smaller than O^{2-} ions (radius = 140 pm) diffuse faster resulting in the comparatively rapid oxidation kinetics by moisture. Thus, the initial reaction involving gaseous oxygen follows a parabolic law which transitions into a linear rate.

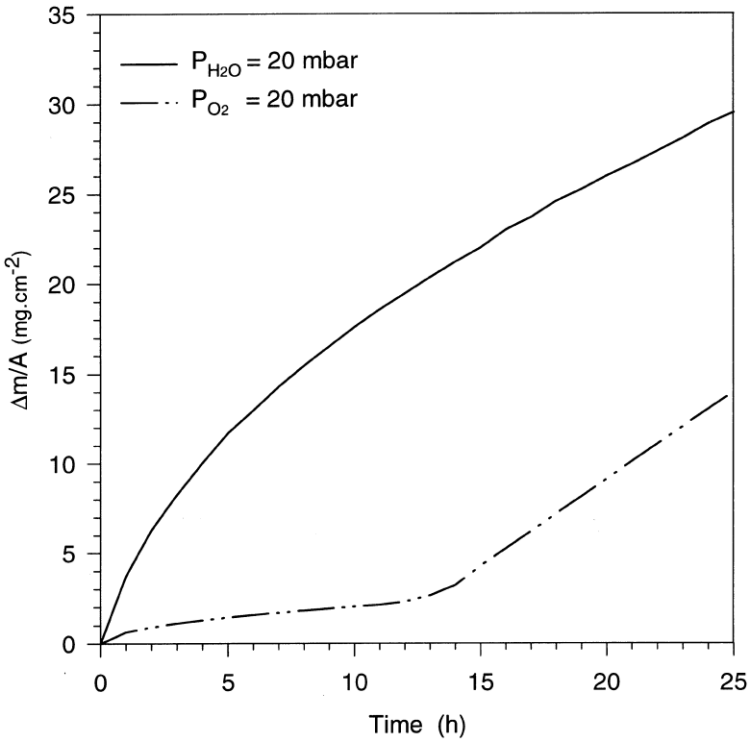

Figure 2.7. Comparison of oxidation of pure titanium at 20 mbar pressure of water vapour with gaseous oxygen (adapted from Wouters et al. [2.63]).

Aluminium is another example of a high-temperature oxidation susceptible metal. Popular alloys used in LPBF AM such as AlSi10Mg can be affected by oxidation from water vapour. Aluminium forms a few nanometer thick overlayer of porous water containing hydroxide ($Al(OH)_3$) and AlOOH over a natural protective alumina (Al_2O_3) layer on its surface. The thickness of the oxide layer can be greater than 1000 nm due to increased humidity and temperature [2.64]. Deng et al. [2.65] proposed oxide thickening occur by the reaction of water with the porous overlayer with alumina to form AlOOH. Then aluminium reduces the AlOOH hydroxide at the interface to create bubbles of H_2

gas. When this hydrogen gas reaches critical pressure, it ruptures the oxide and exposes the reactive aluminium surface for the reaction to propagate. Hence such sensitive metallic powders must be processed and stored properly in anhydrous conditions to avoid oxidation reactions which can be detrimental to the mechanical properties of the produced part.

2.2.3. Volatilisation or evaporation in LPBF AM

Evaporation and formation of a plume are present at the metal laser melt pool in LPBF processes [2.66]. The Langmuir equation (**Equation 2.1**) governs the vaporization fluxes of the alloying elements,

$$J_i = \frac{\lambda P_i}{\sqrt{2\pi M_i T}} \tag{2.1}$$

where J_i is the vapour flux, P_i is vapour pressure over the alloy, M_i is the molecular weight of an element i, T is temperature and λ is a positive fraction accounting for the condensation of some vaporized atoms [2.66]. Thus, some compositional changes due to evaporation are possible in LPBF AM. **Figure 2.8** provides the alloying elements lost due to volatilization for five popular alloys, namely Ti6Al4, SS316, 2.25Cr-1Mo Steel, Incoloy 800H and IN625. Ti6Al4V was found to be most susceptible as it contains aluminium which is volatile (0.922 % of Al loss occurred) [2.66]. The other alloys lost manganese and chromium in lower quantities. Therefore, Superalloy IN 625 (primarily a Ni-Cr alloy), which possesses low amounts of volatile elements had the least loss of alloyants. In LPBF AM the extent of this problem is usually controlled by an appropriate processing parameter to restrict the beam size [2.66], maximum beam temperatures [2.66] and also alloying element measures [2.67].

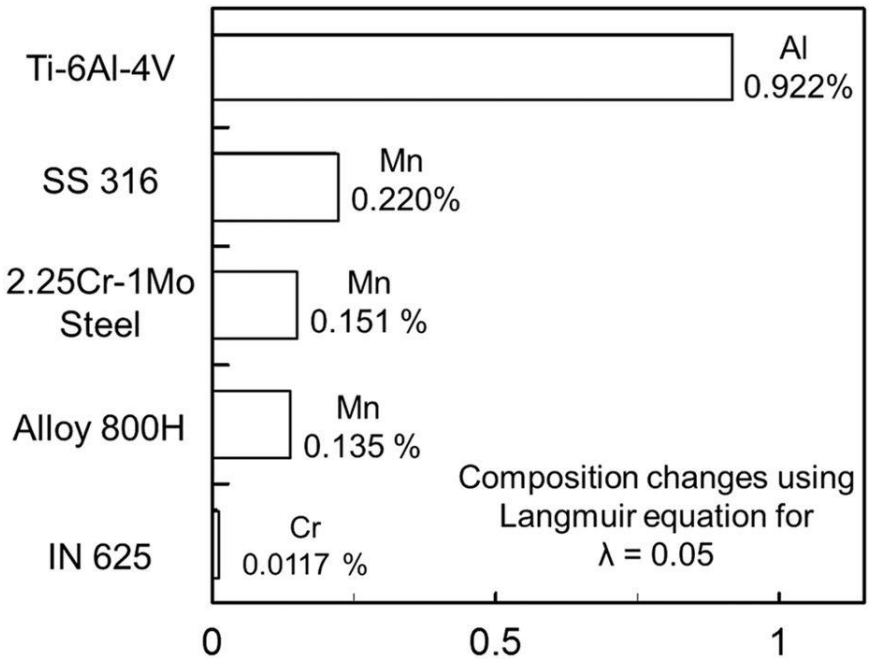

Figure 2.8. Quantity of volatilizing alloying elements for laser processing of Ti6Al4, SS 316, 2.25Cr-1Mo Steel, Incoloy 800H and IN 625 alloys (Adapted from Mukherjee et al. [2.66]).

2.3. Sorption of water

Sorption is a surface phenomenon by which foreign molecules interact with a surface. It must be noted that the sub-surface phenomenon is known as absorption. If a chemical bond due to a reaction is formed with the incoming molecules the phenomenon is known as 'chemisorption' (**Figure 2.9**). If the contaminant adsorbs by physical forces such as Van der Waal's force this phenomenon is called as 'physisorption' (**Figure 2.9**). Generally, on a metal surface, a chemisorbed layer is present underneath a layer of physisorbed molecules.

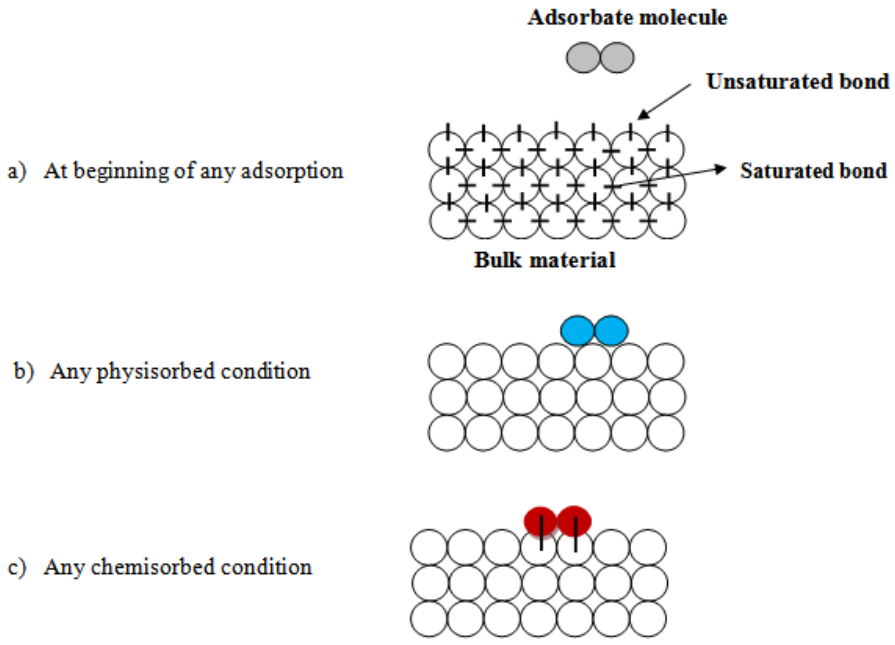

Figure 2.9. A general depiction of (a) Initial stage before adsorption, (b) physisorption and (c) chemisorption of molecules upon a substrate (Adapted from NPTEL website [2.68]).

Sorption can be a reversible process depending upon its nature. Usually, physisorption is reversible upon removal of the bonding forces while chemisorption is irreversible if an irreversible chemical reaction has taken place. Surface sorption can be classified into two categories. The assimilation or uptake on a surface is known as adsorption, the reverse phenomenon, i.e. disintegration from the surface is known as desorption. In many cases, adsorption and desorption can be thought as the forward and backward components of a reversible reaction.

Moisture adsorption is a path to introduce adsorbed water in an LPBF system. This aspect of LPBF AM is not well documented in the literature. Within this work, the sorption of moisture (water) in cellulosic filters in AM was found (Chapter 4) therefore a

brief introduction to the sorption of moisture by natural fibres will be provided. A brief review on moisture sorption on LPBF AM metallic powder surfaces has also been detailed.

2.3.1. Sorption of water by natural fibres

Natural fibres are plant-based polymers composed of organic molecules for example cellulose, hemicellulose, pectin and lignin. Filter paper used for air filters in the automobile, industrial air cleaning and AM (including LPBF) for air purification is generally composed of cellulose, hence it's a subject of interest. Natural fibres such as jute, coir, sisal and products from natural fibres (such as filter paper) adsorb water [2.69]. It occurs due to the presence of hydrophilic (mainly hydroxide) groups on the cell wall [2.70] of the fibres [2.69]. Fibre swelling occurs as the fibres absorb moisture. Water sorption on the natural fibre surface is reversible with changing Relative Humidity (RH) [2.69]. These adsorption and desorption processes can be measured by Dynamic Vapor sorption (DVS) experiments (discussed in detail in Chapter 3). **Figure 2.10** (a, b) displays the adsorption and desorption data for cotton, filter paper, flax, hemp, jute and sisal fibres [2.69]. The shape of the isotherms is sigmoidal (IUPAC type 2) for all the investigated natural fibres. However, the quantity of moisture adsorbed depends on the material of natural fibre. **Figure 2.10**. (c) compares flax and duralin fibres and a clear presence of hysteresis are visible [2.72]. It shows that the desorption lags adsorption in response to the same change in relative humidity. The available physical explanations of the sigmoidal isotherm shape and the hysteresis phenomenon are still not widely accepted [2.71].

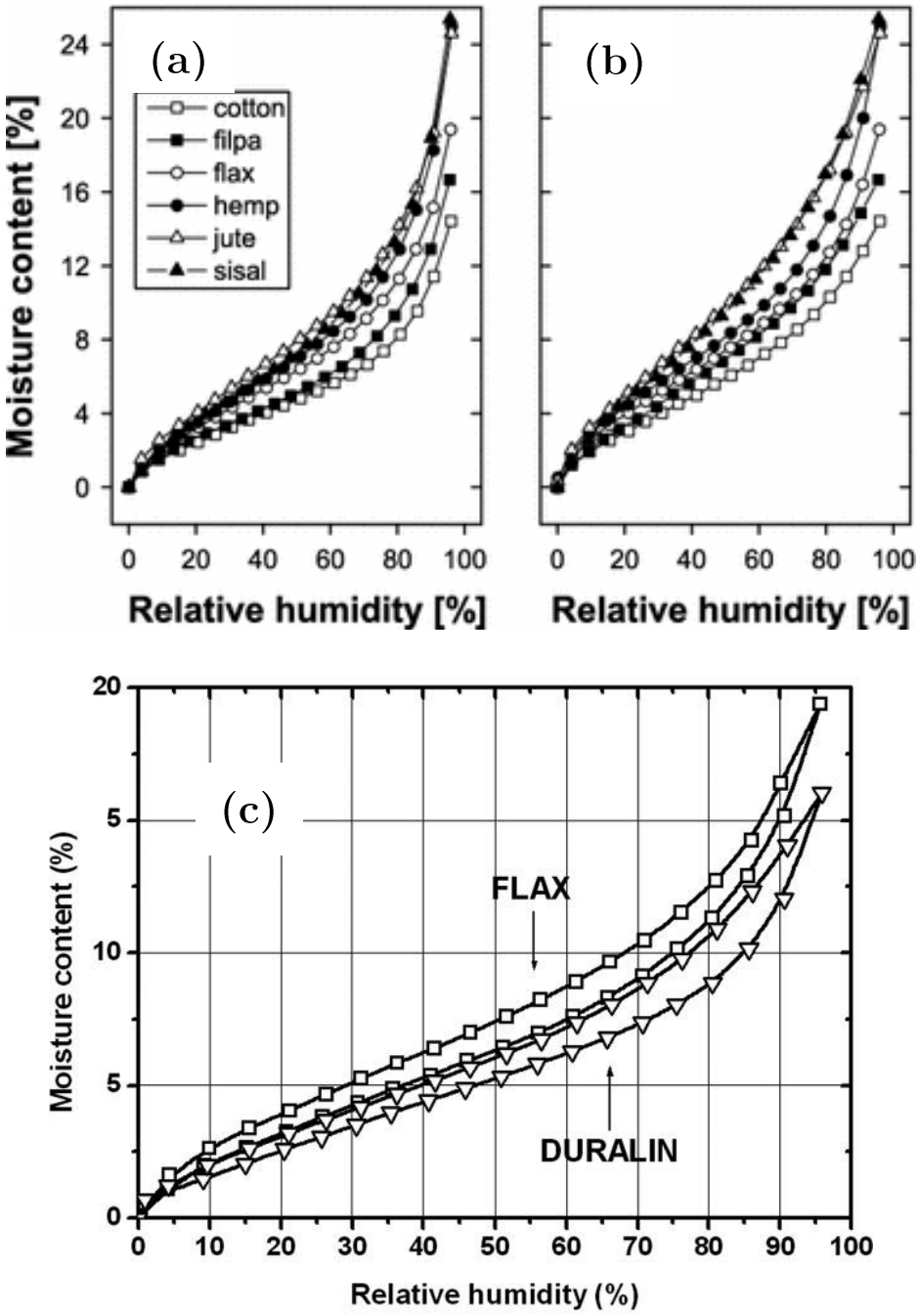

Figure 2.10. Equilibrium moisture content of natural fibres in the full set RH range during the (a) adsorption, (b) desorption processes in the sorption isotherm loops for cotton, filter paper, flax, hemp, jute and sisal fibres (Adapted from Xie et al. [2.69]) and (c) comparison of sorption isotherm loops for flax and duralin fibres (Adapted from Hill et al. [2.72]).

Adsorption and desorption of water on natural fibres follow the parallel exponential kinetics (PEK) model. The PEK consists of a double exponential equation as given below in **Equation 2.2.**

$$MC = MC_0 + MC_1(1 - e^{t/t_1}) + MC_2(1 - e^{t/t_2}) \quad (2.2)$$

here MC (% of weight change) represents the moisture content of a sample exposed to a particular RH value at the isothermal condition as a function of time, MC_0 (%) is the initial moisture content, the exponential terms represent a slow and a fast process respectively. MC_1 (%) and MC_2 (%) are constants representing the moisture content associated with infinite times and t_1 and t_2 are also constants representing the characteristic or effective times required to reach them. Thus, any adsorption or desorption contains both a fast and a slow step occurring concurrently. **Figure 2.11** depicts both the fast step, slow step and the overall adsorption kinetics for a flax fibre exposed to 65 % RH within a DVS machine chamber. The experimental data can be fitted using the PEK with a high coefficient of correlation (R^2).

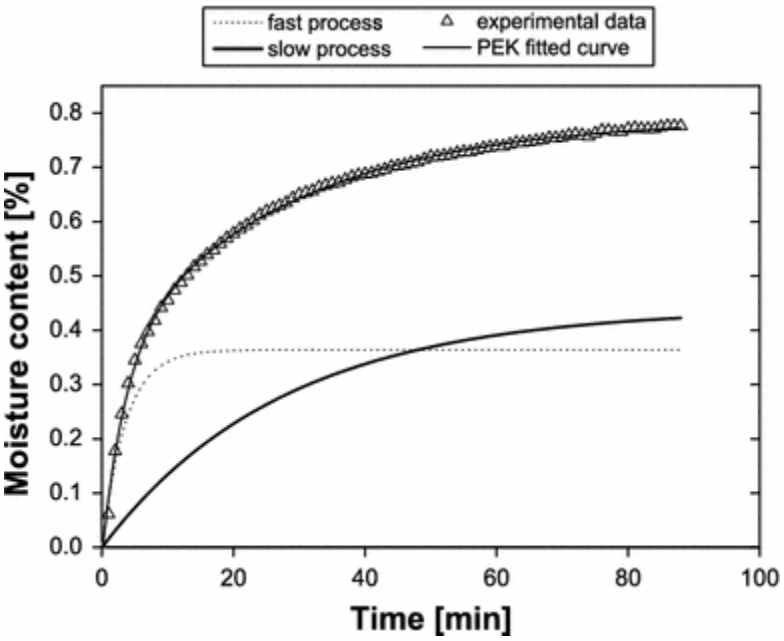

Figure 2.11. Example of PEK curve fitting to experimental adsorption data (open triangles) of hemp fibre at 65 % target RH, the fitted curves (lines) showing the slow and fast parallel exponential kinetic processes, and the sum of fast and slow processes (Adapted from Xie et al. [2.69]).

2.3.2. Sorption of water on metallic surfaces

Water sorption also occurs on metallic surfaces including fine powders having high specific surface area used in LPBF AM. Thus, moisture sorption on powder surfaces occurs in a humid environment. For LPBF AM, only a few research articles are available on this subject. Thus, a complete understanding is still lacking. Dynamic vapor sorption (DVS) has also been used for determining water (moisture) adsorption on metallic powders. Using DVS on 3 batches of AlSi7Mg powders (refer **Table 2.5** for PSD comparison) Muniz-Lerma et al. [2.73] detailed sorption isotherm loops for moisture (**Figure 2.12**). Powders A and B have relatively similar size distribution whereas Powder C has more

fines. **Figure 2.12** (a, b) reveals that the nature of moisture sorption for Powders A and B are similar. Powder C had more fines thus had a larger moisture amount of sorption. Upon removal of the fines from Powder C by sieving the moisture sorption decreases (**Figure 2.12** (c, d)).

Table 2.5. Particle size distribution of the tested powders batches A, B, and C (Adapted from Muniz-Lerma et al. [2.73]).

Powder	D_{10} (µm)	D_{50} (µm)	D_{90} (µm)	S_w
Powder A	48	63	83	10.6
Powder B	54	70	91	10.8
Powder C	14	31	58	4.2

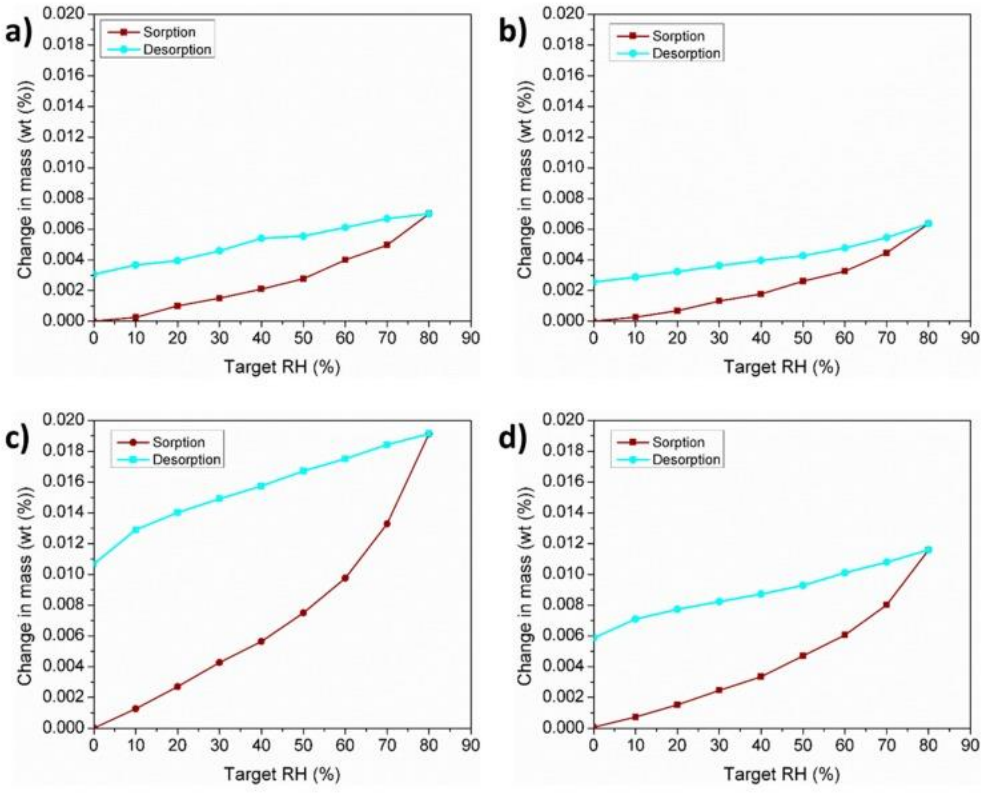

Figure 2.12. Dynamic vapor sorption (DVS) isotherms for (a) Powder A, (b) powder B, (c) powder C, and (d) sieved powder C (Adapted from Muniz-Lerma et al. [2.73]).

Sartin et al. [2.74] characterised 316L stainless steel virgin and reused powders using Karl Fischer titration [2.75]. The maximum sorption was found to be 0.092 wt.% thus it was deemed to be negligible. Murphy et al. [2.76] characterised Ti6Al4V powders using weight loss on drying to obtain the moisture content for powders stored for several months. Although three batches of Ti6Al4V with different powder sizes was used the moisture loss was constant at around 0.1 wt. %. Cordova et al. [2.77] stored, Inconel 718, Ti6Al4V, AlSi10Mg, and Scalmalloy powders for 72 hours at 50 °C at 90 % RH. The moisture sorption measured by mass loss on drying was found to be the most for AlSi10Mg (~0.12 wt.%), with the other powders sorbing lesser amounts of moisture (<0.06 wt.%). Comparison of the oxygen peak ($O_{K\alpha}$) using energy dispersive x-ray (EDX) spectroscopy before and after the moisture storage treatment is presented in **Table 2.6**.

Although EDX peaks is an inaccurate method to determine composition, the increase in oxygen for AlSi10Mg is notable. It indicates a presence of chemical oxidation due to moisture occurring at low temperatures. This can be detrimental to the powder properties and confirms the necessity of additional care to reduce powder contact with water vapour during powder production and handling for some susceptible powders like AlSi10Mg or the AlSi family.

Table 2.6. Oxygen content (Kα) ratio of powders stored in moisture to as received Inconel 718, Ti6Al4V, AlSi10Mg and Scalmalloy powders (Adapted from Cordova et al. [2.77]).

Material	Kα peak ratio (Moisturized / As received)
Inconel 718	2.2
Ti6Al4V	1.5
AlSi10Mg	3.1
Scalmalloy	1.6

Water vapour (moisture) sorption results depend on the instrument used, experimental conditions (time of storage, presence of heating, etc.), type of powder and presence of reactions. Humidity has been treated as an 'uncontrollable factor' in powder handling and recycling [2.78]. Therefore, it can affect powders during handling, processing and storage for LPBF AM.

2.4. References

[2.1] Wang, F. Mechanical property study on rapid additive layer manufacture Hastelloy® X alloy by selective laser melting technology. *Int J Adv Manuf Technol* **58**, 545–551 (2012).

[2.2] Li, J. & Wang, H. M. Microstructure and mechanical properties of rapid directionally solidified Ni-base superalloy Rene′41 by laser melting deposition manufacturing. *Materials Science and Engineering: A* **527**, 4823–4829 (2010).

[2.3] Basak, A., Acharya, R. & Das, S. Additive Manufacturing of Single-Crystal Superalloy CMSX-4 Through Scanning Laser Epitaxy: Computational Modeling, Experimental Process Development, and Process Parameter Optimization. *Metallurgical and Materials Transactions A* **47**, 3845–3859 (2016).

[2.4] Zhang, H. *et al.* Selective laser melting of rare earth element Sc modified aluminum alloy: Thermodynamics of precipitation behavior and its influence on mechanical properties. *Additive Manufacturing* **23**, 1–12 (2018).

[2.5] Liu, L. *et al.* Rare Earth Element Yttrium Modified Mg-Al-Zn Alloy: Microstructure, Degradation Properties and Hardness. *Materials* **10**, 477 (2017).

[2.6] Urban, N., Meyer, A., Kreitlein, S., Leicht, F., & Franke, J. Efficient near net-shape production of high-energy rare-earth magnets by laser beam melting. In *Applied Mechanics and Materials* **871**, 137-144 (2017).

[2.7] Iveković, A. *et al.* Selective laser melting of tungsten and tungsten alloys. *International Journal of Refractory Metals and Hard Materials* **72**, 27–32 (2018).

[2.8] Tarasova, T. V., Nazarov, A. P. & Shalapko, Yu. I. Abrasive and fretting wear resistance of refractory cobalt alloy specimens manufactured by the method of selective laser melting. *J. Frict. Wear* **35**, 365–373 (2014).

[2.9] Sing, S. L., Wiria, F. E. & Yeong, W. Y. Selective laser melting of titanium alloy with 50 wt% tantalum: Effect of laser process parameters on part quality. *International Journal of Refractory Metals and Hard Materials* **77**, 120–127 (2018).

[2.10] Library of Congress Collections. STL (STereoLithography) File Format Family. Available at: https://www.loc.gov/preservation/digital/formats/fdd/fdd000504.shtml. (Accessed: 2nd March 2020).

[2.11] Haeri, S., Wang, Y., Ghita, O. & Sun, J. Discrete element simulation and experimental study of powder spreading process in additive manufacturing. *Powder Technology* **306**, 45–54 (2017).

[2.12] Calignano, F. Investigation of the accuracy and roughness in the laser powder bed fusion process. *Virtual and Physical Prototyping* **13**, 97–104 (2018).

[2.13] Dawes, J., Bowerman, R. & Trepleton, R. Introduction to the Additive Manufacturing Powder Metallurgy Supply Chain. *Johnson Matthey Technol Rev* **59**, 243–256 (2015).

[2.14] Simonelli, M. *et al.* A Study on the Laser Spatter and the Oxidation Reactions During Selective Laser Melting of 316L Stainless Steel, Al-Si10-Mg, and Ti-6Al-4V. *Metall and Mat Trans A* **46**, 3842–3851 (2015).

[2.15] Grainger, L. Understanding the effects of metal powder reuse in laser powder-bed fusion AM. in *Proceedings of Fraunhofer direct digital manufacturing conference* (2018).

[2.16] Renishaw plc. RenAM 500Q. Available at: http://www.renishaw.com/en/renam-500q--42781. (Accessed: 2nd March 2020)

[2.17] GE Additive. X LINE 2000R. Available at: https://www.ge.com/additive/additive-manufacturing/machines/dmlm-machines/x-line-2000r. (Accessed: 2nd March 2020)

[2.18] EOS. EOS P 500 - industrial 3D printing for plastic parts. Available at: https://www.eos.info/systems_solutions/eos-p-500. (Accessed: 2nd March 2020)

[2.19] Vock, S., Klöden, B., Kirchner, A., Weißgärber, T. & Kieback, B. Powders for powder bed fusion: a review. *Progress in Additive Manufacturing* **4**, 383–397 (2019)

[2.20] Sun, P., Fang, Z. Z., Xia, Y., Zhang, Y. & Zhou, C. A novel method for production of spherical Ti-6Al-4V powder for additive manufacturing. *Powder Technology* **301**, 331–335 (2016).

[2.21] Nguyen, Q. B. *et al.* Characteristics of Inconel Powders for Powder-Bed Additive Manufacturing. *Engineering* **3**, 695–700 (2017).

[2.22] Taheri, H., et al. Powder based additive manufacturing-A review of types of defects, generation mechanisms, detection, property evaluation and metrology. *Int. J. Addit. Subtractive Mater. Manuf.* ***1***, 172-209 (2017).

[2.23] Chen, G. *et al.* A comparative study of Ti-6Al-4V powders for additive manufacturing by gas atomization, plasma rotating electrode process and plasma atomization. *Powder Technology* **333**, 38–46 (2018).

[2.24] Anderson, I. E., White, E. M. H. & Dehoff, R. Feedstock powder processing research needs for additive manufacturing development. *Current Opinion in Solid State and Materials Science* **22**, 8–15 (2018).

[2.25] Susan, D. F., Puskar, J. D., Brooks, J. A. & Robino, C. V. Porosity in stainless steel LENS powders and deposits (No. SAND2000-1993C). *Sandia National Labs., Albuquerque, NM (US)*

[2.26] Medina, F. Reducing metal alloy powder costs for use in powder bed fusion additive manufacturing: Improving the economics for production. (The University of Texas at El Paso, 2013).

[2.27] Tekna. Spheroidization Systems. Available at: http://www.tekna.com/spheroidization-systems. (Accessed: 2nd March 2020)

[2.28] Sun, Y. Y. *et al.* Manipulation and Characterization of a Novel Titanium Powder Precursor for Additive Manufacturing Applications. *JOM* **67**, 564–572 (2015).

[2.29] Gai, G., Yang, Y., Jin, L., Zou, X. & Wu, Y. Particle shape modification and related property improvements. *Powder Technology* **183**, 115–121 (2008).

[2.30] Yablokova, G. *et al.* Rheological behavior of β-Ti and NiTi powders produced by atomization for SLM production of open porous orthopedic implants. *Powder Technology* **283**, 199–209 (2015).

[2.31] Granutools. Cohesive Index | Powder Cohesive Index, Powder Rheometer. Available at: https://granutools.com/products/granudrum/. (Accessed 2nd March 2020)

[2.32] Boschini, F., Delaval, V., Traina, K., Vandewalle, N. & Lumay, G. Linking flowability and granulometry of lactose powders. *Int J Pharm* **494**, 312–320 (2015).

[2.33] Murr, L. E. Metallurgy of additive manufacturing: Examples from electron beam melting. *Additive Manufacturing* **5**, 40–53 (2015).

[2.34] Gong, X., Cheng, B., Price, S., & Chou, K. Powder-bed electron-beam-melting additive manufacturing: powder characterization, process simulation and metrology. *Early Career Technical Conference, Birmingham, AL.* 55-66 (2013).

[2.35] Arce, A. N. Thermal Modeling and Simulation of Electron Beam Melting for Rapid Prototyping on Ti6Al4V Alloys. (North Carolina State University, 2012).

[2.36] Bourell, D., Stucker, B., Spierings, A. B., Herres, N., & Levy, G. Influence of the particle size distribution on surface quality and mechanical properties in additive manufactured stainless-steel parts. *Rapid Prototyping Journal* **17**, 195-202 (2011).

[2.37] Badrossamay, M., Yasa, E., Van Vaerenbergh, J. & Kruth, J.-P. Improving Productivity Rate in SLM of Commercial Steel Powders. *Technical Paper - Society of Manufacturing Engineers*. **09,** 1–13 (2009).

[2.38] Liu, B., Wildman, R., Tuck, C., Ashcroft, I. & Hague, R. Investigation the effect of particle size distribution on processing parameters optimisation in selective laser melting process. *Additive manufacturing research group, Loughborough University* 227–238 (2011).

[2.39] Abd-Elghany, K. & Bourell, D. L. Property evaluation of 304L stainless steel fabricated by selective laser melting. *Rapid Prototyping Journal* **18**, 420–428 (2012).

[2.40] Li, R. *et al.* Densification behavior of gas and water atomized 316L stainless steel powder during selective laser melting. *Applied Surface Science* **256**, 4350–4356 (2010).

[2.41] Lutter-Günther, M., Hofmann, A., Hauck, C., Seidel, C. & Reinhart, G. Quantifying Powder Losses and Analyzing Powder Conditions in order to Determine Material Efficiency in Laser Beam Melting. *AMM* **856**, 231–237 (2016).

[2.42] Kellens, K. *et al.* Energy and Resource Efficiency of SLS/SLM Processes (Keynote Paper). *SFF Symposium.* 1–16 (2011).

[2.43] Gebbe, C., Lutter-Günther, M., Greiff, B., Glasschröder, J. & Reinhart, G. Measurement of the Resource Consumption of a Selective Laser Melting Process. *AMM* **805**, 205–212 (2015).

[2.44] Kappes, B., Moorthy, S., Drake, D., Geerlings, H. & Stebner, A. Machine Learning to Optimize Additive Manufacturing Parameters for Laser Powder Bed Fusion of Inconel 718. *Proceedings of the 9th International Symposium on Superalloy 718 & Derivatives: Energy, Aerospace, and Industrial Applications (eds. Ott, E. et al.)* 595–610 (2018).

[2.45] Ardila, L. C. *et al.* Effect of IN718 Recycled Powder Reuse on Properties of Parts Manufactured by Means of Selective Laser Melting. *Physics Procedia* **56**, 99–107 (2014).

[2.46] Barnhart, B. K. Characterization of Powder and the Effects of Powder Reuse in Selective Laser Melting. (2017).

[2.47] Leung, C. L. A. *et al.* The effect of powder oxidation on defect formation in laser additive manufacturing. *Acta Materialia* **166**, 294–305 (2019).

[2.48] Del Re, F. *et al.* Statistical approach for assessing the effect of powder reuse on the final quality of AlSi10Mg parts produced by laser powder bed fusion additive manufacturing. *Int J Adv Manuf Technol* **97**, 2231–2240 (2018).

[2.49] Cordova, L., Campos, M. & Tinga, T. Revealing the Effects of Powder Reuse for Selective Laser Melting by Powder Characterization. *JOM* **71**, 1062–1072 (2019).

[2.50] Maamoun, A. H., Elbestawi, M., Dosbaeva, G. K. & Veldhuis, S. C. Thermal post-processing of AlSi10Mg parts produced by Selective Laser Melting using recycled powder. *Additive Manufacturing* **21**, 234–247 (2018).

[2.51] Leicht, A. Aspects of building geometry and powder characteristics in powder bed fusion. 43.

[2.52] Geisert, S., Fischer, J., Klosch-Trageser, M. & Stolpe, M. Powder production processes—optimizing parameters for the generation of fine metal powders for additive manufacturing. *Proceedings of Fraunhofer direct digital manufacturing conference* (2018).

[2.53] Jacob, G., Jacob, G., Brown, C. U., Donmez, M. A., Watson, S. S., & Slotwinski, J. Effects of powder recycling on stainless steel powder and built material properties in metal powder bed fusion processes. *US Department of Commerce, National Institute of Standards and Technology.* (2017)

[2.54] O'Leary, Richard, Rossi Setchi, Paul Prickett, and Gareth Hankins. "An investigation into the recycling of Ti-6Al-4V powder used within SLM to improve sustainability." *Impact: The Journal of Innovation* **8**, 377 (2016).

[2.55] Seyda, V., Kaufmann, N. & Emmelmann, C. Investigation of Aging Processes of Ti-6Al-4 V Powder Material in Laser Melting. *Physics Procedia* **39**, 425–431 (2012).

[2.56] Vock, S., Hartel, M., Maiwald-Immer, T., Wendt, F. & Burghardt, K. Powder assessment for powder bed based additive manufacturing. in *Proceedings of Fraunhofer direct digital manufacturing conference* (2018).

[2.57] Hooper, P. A. Melt pool temperature and cooling rates in laser powder bed fusion. *Additive Manufacturing* **22**, 548–559 (2018).

[2.58] Finlay, W. L. & Snyder, J. A. Effects of three interstitial solutes (nitrogen, oxygen, and carbon) on the mechanical properties of high-purity, alpha titanium. *JOM* **2**, 277–286 (1950).

[2.59] Bauer, D. *et al.* Effect of process gas and powder quality on aluminum alloys processed by laser based powder bed melting process. in 8–10 (2016).

[2.60] Vanmeensel, K. *et al.* Additively manufactured metals for medical applications. *Additive Manufacturing* 261–309 (2018).

[2.61] Chemistry LibreTexts. 8.8A: Ellingham Diagrams. Available at: https://chem.libretexts.org/Bookshelves/Inorganic_Chemistry/Map%3A_Inorganic_Chemistry_(Housecroft)/08%3A_Reduction_and_oxidation/8.8%3A_Applications_of_Redox_Reactions_to_the_Extraction_of_Elements_from_their_Ores/8.8A%3A_Ellingham_Diagrams. (Accessed: 2nd March 2020)

[2.62] Murray, J. L. & Wriedt, H. A. The O—Ti (Oxygen-Titanium) system. *JPE* **8**, 148–165 (1987).

[2.63] Wouters, Y., Galerie, A. & Petit, J.-P. Thermal oxidation of titanium by water vapour. *Solid State Ionics* **104**, 89–96 (1997).

[2.64] Bauer, D. M. *et al.* Investigations of aging behaviour for aluminium powders during an atmosphere simulation of the LBM process. *Powder Metallurgy* **60**, 175–183 (2017).

[2.65] Deng, Z.-Y., Ferreira, J. M. F., Tanaka, Y. & Ye, J. Physicochemical Mechanism for the Continuous Reaction of γ-Al2O3-Modified Aluminum Powder with Water. *Journal of the American Ceramic Society* **90**, 1521–1526 (2007).

[2.66] Mukherjee, T., Zuback, J. S., De, A. & DebRoy, T. Printability of alloys for additive manufacturing. *Scientific Reports* **6**, 1-8 (2016).

[2.67] Zenou, M. & Grainger, L. Additive manufacturing of metallic materials. *Additive Manufacturing* 53–103 (2018).

[2.68] NPTEL. Lecture 2: Adsorption in catalysis. Available at: https://nptel.ac.in/courses/103103026/module1/lec2/2.html. (Accessed: 2nd March 2020)

[2.69] Hill, C. A. S. & Xie, Y. The dynamic water vapour sorption properties of natural fibres and viscoelastic behaviour of the cell wall: is there a link between sorption kinetics and hysteresis? *Journal of Materials Science* **46**, 3738–3748 (2011).

[2.70] Britannica. cell wall | Description, Properties, Components, & Communication | Available at: https://www.britannica.com/science/cell-wall-plant-anatomy. (Accessed: 2nd March 2020)

[2.71] Hill, C. A. S., Norton, A. & Newman, G. The water vapor sorption behavior of natural fibers. *Journal of Applied Polymer Science* **112**, 1524–1537 (2009).

[2.72] Hill, C. A. S., Norton, A. J. & Newman, G. The water vapour sorption properties of Sitka spruce determined using a dynamic vapour sorption apparatus. *Wood Sci Technol* **44**, 497–514 (2010).

[2.73] Muñiz-Lerma, J., Nommeots-Nomm, A., Waters, K. & Brochu, M. A Comprehensive Approach to Powder Feedstock Characterization for Powder Bed Fusion Additive Manufacturing: A Case Study on AlSi7Mg. *Materials* **11**, 2386 (2018).

[2.74] Sartin, B., et al. "316L powder reuse for metal additive manufacturing." *Proceedings of the 28th Annual International Solid Freeform Fabrication Symposium*, 351-364 (2017).

[2.75] Azo Materials. What Is Karl Fischer Titration and What Are Its Applications? Available at: https://www.azom.com/article.aspx?ArticleID=16017. (Accessed: 2nd March 2020)

[2.76] Murphy, T. F. & Schade, C. T. 6 - Measurement of powder characteristics and quality for additive manufacturing in aerospace alloys. *Additive Manufacturing for the Aerospace Industry* (eds. Froes, F. & Boyer, R.) 99–142 (2019).

[2.77] Cordova, L., Campos, M., & Tinga, T. Assessment of Moisture Content and Its Influence on Laser Beam Melting Feedstock. *Proceedings of the Euro PM2017 Congress & Exhibition: European Annual Powder Metallurgy congress and exhibition, Milan, Italy*. 1-5 (2017, October).

[2.78] Lovejoy, T. R., Muetterties, N. K., & Otsu, D. T. Metals Additive Manufacturing Powder Aging Characterization. (2016).

Chapter 3

Experimental Methodology

This chapter details the specifics of the experiments carried during this research work. It consists of two sections which correspond to the experiments required for chapter 4 and chapter 5. Section 3.1 details the experiments used to characterize filter paper from a commercial Hengst E1900L air filter (Hengst, Germany). Details for hygrometry within the LPBF equipment have also been described. Section 3.2 describes the experiments required to characterize Grade 23 Ti6Al4V powder (Tekna, Canada) and evaluate the effect of storage in a humid environment. The flowchart is shown in **Figure 3.1** details the properties sought, and the experimental techniques used for characterization. The primary goal is to identify and quantify moisture sources in LPBF AM.

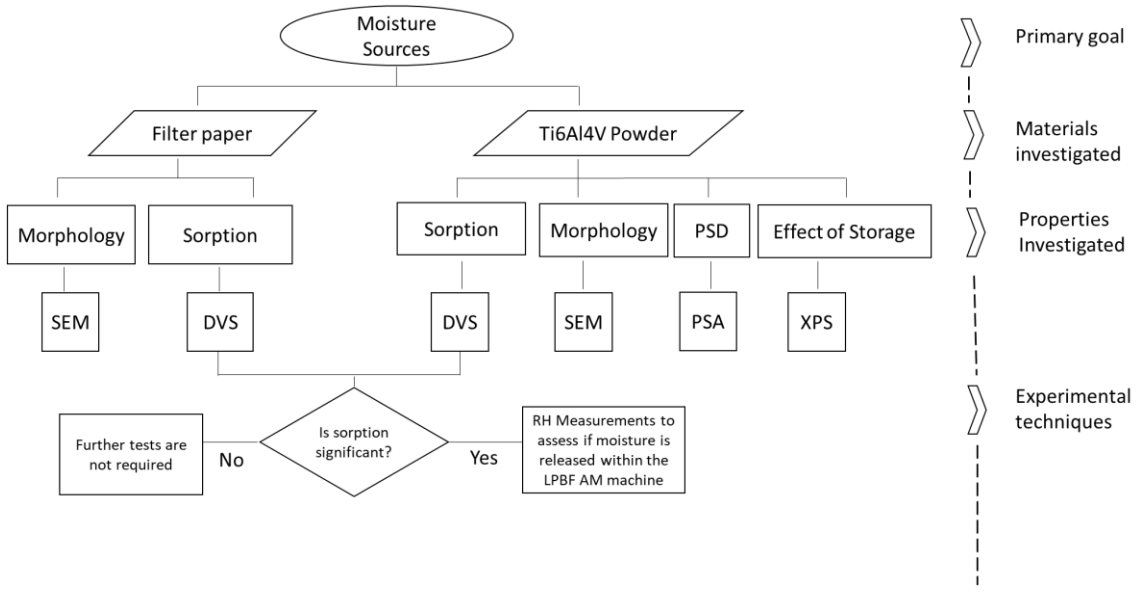

Figure 3.1. Flowchart detailing objectives and experimental decisions for this work.

3.1. Experimental methodology for Chapter 4

3.1.1. Dynamic Vapor Sorption of filter paper

Vapour sorption properties of filter paper were quantified using dynamic vapour sorption (DVS). The experiments allow to study and understand the behaviour of moisture sorption of filter paper with varying RH. The DVS data was also used for calculations of moisture quantities within a filter.

Instrumental operation principle

DVS is a technique that measures the changing weight of a sample with respect to change in atmospheric RH content. DVS Intrinsic Plus [3.1] (Sorption Measurement Systems, UK) was used for this study. **Figure 3.2** shows the schematic of a dynamic vapour sorption unit [3.2]. The inner chamber uses a precise microbalance with one weighing pan for the sample with a second pan for reference. An inert carrier gas such as nitrogen, argon or dry air is generally used to deliver water vapour within the closed system. Moist carrier gas flow is controlled by mass flow controllers as shown in **Figure 3.2** into the system. When the target value of RH is reached, the valves allowing the moist carrier gas closes. The sequence of RH change or control of RH change is programmable according to the needs of the experiment. Thus, both an RH increment-decrement loop (known as the sorption isotherm loop) or a static value of RH can be maintained within the chamber. If required, the specimen chamber may be heated up to a certain temperature.

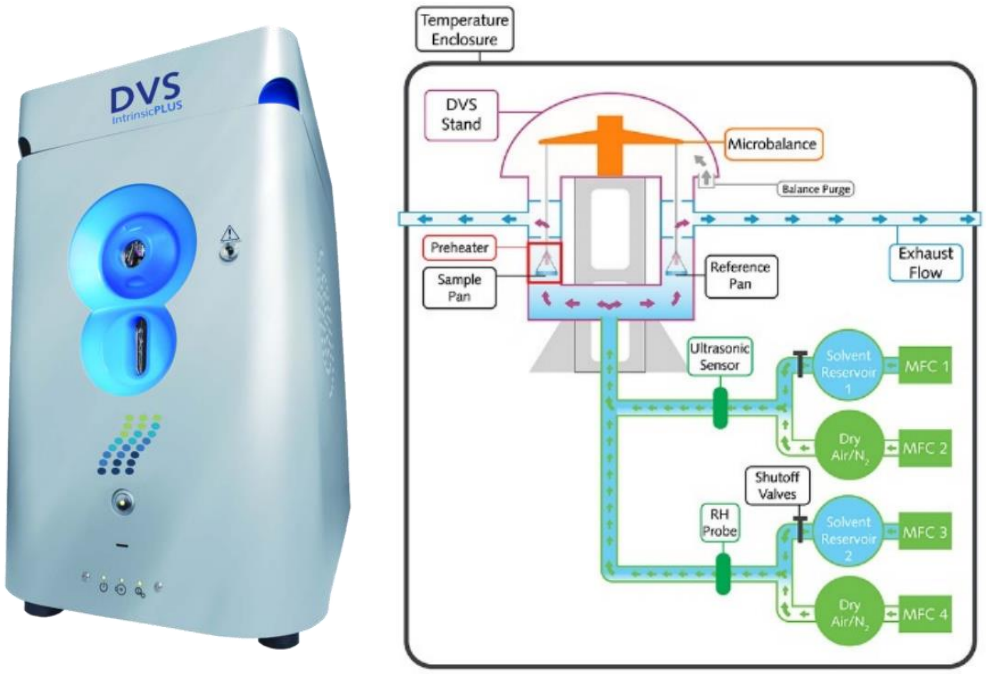

Figure 3.2. (a) Exterior view and (b) working principle schematic of dynamic vapour sorption system (Adapted from sorption measurement systems website [3.2]).

Experimental setup and process

For this work, the DVS intrinsic was used with nitrogen as the carrier gas to generate a sorption isotherm loop which was measured and repeated once for filter paper. DVS samples are required to be under a gram in mass and should fit within the pan (< 2 inches in diameter) within the measurement chamber. Filter samples (diameter 1.5 inches) were punched using an APSCO 330A paper punch and used for DVS. **Figure 3.3** details a schematic of the programmed sorption isotherm loop; a description of an experiment includes,

- Initial drying of the sample under flowing air for six hours.
- The mass of the sample was considered as the reference mass.
- The RH was raised by a step of 10 %.

- The mass of the sample increased in response and was considered to stabilise when the rate of change in mass (dm/dt) was less than 0.002 %.
- After stabilisation, the RH within the system was raised by another 10 %. Again, stabilisation occurred, and this cycle was continued until it reaches 80 % RH.
- After attaining 80 % RH and as the sample mass stabilises, the RH was reduced in steps of 10 % RH. The mass change was assumed to be complete when the rate of change in mass (dm/dt) is less than 0.002 %.
- This was continued until the sample mass had stabilised at 0 % RH.

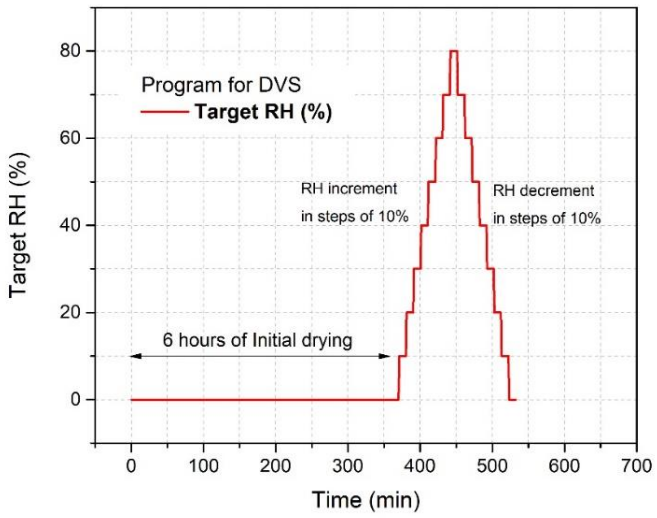

Figure 3.3. Program for the DVS sorption isotherm loop.

3.1.2. In-situ Hygrometry in LPBF AM

RH is generally not measured within the build chamber of LPBF AM equipment. To detect the presence of water vapour within the build chamber in-situ hygrometry was performed.

Instrumental operation principle

In-situ measurement of humidity was conducted within the LPBF AM chamber during this study. A Traceable Memory Hygrometer (Fisher Scientific, USA) with a probe was utilized. It uses a resistive polymer film sensor for monitoring RH [3.3]. The instrument has been rated and pre-calibrated to measure from 10-95 % RH with a sensitivity of 0.1 % RH. Verification in an evacuated glove box (RH ~ 0) was conducted. The hygrometer reported 0.1 % RH at this state. Assuming the RH in the evacuated glove box was approximately zero, the reported resolution of the instrument was confirmed.

Experimental setup and process

The hygrometer probe was mounted inside the LPBF chamber (Renishaw AM 250) as shown in **Figure 3.4**. This allowed in-situ measurements of RH within the LPBF system.

Figure 3.4. External view of the mounted probe hygrometer displaying the RH inside the build chamber of a Renishaw AM 250 LPBF unit.

RH measurements within the LPBF AM were conducted with various filter and atmospheric preparation conditions. The Renishaw AM 250 can be operated in two different chamber atmosphere preparation methods. The first method denominated as "with evacuation", consists of an evacuation step followed by a purging process. The evacuation step consists of pumping out the gases present in the build chamber using a mechanical vacuum pump until a vacuum of 40 mBar is reached. The purging process was carried out by filling the build chamber with Ar gas followed by the simultaneous injection and venting of Ar (will be referred to as purge/vent) until the target oxygen concentration in the chamber was reached. The second chamber atmosphere preparation method denoted as "without evacuation", lacks an evacuation step. Only presents a purging process is carried out until the target oxygen concentration was reached. In both methods, periodic gas recirculation through the filter occurred during the purging process. When the target concentration of oxygen was reached, gas recirculation was continuous until the printing process started. The set of experiments (reported in Chapter 4) was

designed to study the effect of varying filter conditions on the two-different chamber atmosphere preparation methods.

In this set of experiments, both methods, “with evacuation” and “without evacuation”, were used with a gas recirculation time of 5 minutes after 1000 ppm of oxygen concentration was reached. Three filter conditions were tested by both chamber atmosphere preparation methods for a total of six testing conditions (**Table 3.1**) as follows, in order to identify a baseline value of RH. The first pair of the tests consisted of the chamber atmosphere preparation methods were conducted without a filter. The second pair of tests were conducted using filters dried at 90 °C for 5 hr. Finally, the third pair of tests was performed using as-received filters stored under laboratory environment and denominated as ‘non-dried filter’.

Table 3.1. Experiments with three filter conditions.

Filter Conditioning	Atmospheric preparation conditions
Non-Dried Filter	1. Single evacuation cycle. (referred as without evacuation) 2. Single evacuation cycle with purge/vent. (referred as with evacuation)
Dried Filter	
Without Filter	

3.1.3. Morphology of Filter Paper

Filter paper is made from cellulosic fibres. The morphology is important to describe how it can adsorb moisture from the atmosphere and then can act as a moisture source in LPBF AM.

Instrumental operation principle

The morphology of the filter paper was studied using a variable pressure Hitachi SU3500 (Hitachi, Japan) Scanning Electron Microscope (SEM). The SEM directs electrons on samples within an evacuated chamber to generate various output fundamental particles (or waves) such as electrons and x-rays. Secondary electrons generated by inelastic collisions of the directed electrons with the electrons of the atoms at the sample surface are detected. These secondary electrons come from the sample surface depth of approximately < 10 nm and provide topographic information. Elastic scattering of the electrons generates backscattered electrons (BSE) from deeper sites of the specimen. BSE provides information on sample topography and compositional contrast. Since larger atoms have a larger probability of elastic collisions, the brighter sections of a BSE image correspond to the presence of an element with a higher atomic number. With the Hitachi SU3500 SEM, images at maximum resolution 7 nm (at 3 kV) and 10 nm (at 5 kV) can be obtained for secondary and backscattered electrons respectively [3.4]. The other fundamental particles offer more information about the specimen. For example, the generated X rays can be analysed to generate compositional data.

Experimental setup and process

Small filter samples were cut and fixed to aluminium holder on carbon tape. Samples were analysed using secondary electrons in the SEM. The experimental setup used to the pressure of 70 Pa, under 10 kV of accelerating voltage.

3.1.4. Specific surface area of filter paper

Filter paper is made of wound cellulosic fibres. As it allows a considerable specific surface (surface area per unit mass) for water vapour (moisture) adsorption, it is important to obtain its numeric value.

Instrumental operation principle

The specific surface area was measured for filter paper using the Brunauer-Emmett-Teller (BET) technique [3.5]. A Micromeritics TriStar 3000 (Micromeritics Instrument Corporation, USA) gas sorption system was used to measure the specific surface area of the filter paper. This technique consists of measurement of the pressure change on adsorption of an inert adsorbate gas (usually krypton, argon or nitrogen) on a clean adsorbent surface at low temperatures (usually at 77.3 K, boiling point of N_2 at 1 atm). The pressure change can be related to the quantity of gas adsorption using **Equation 3.1**.

$$\frac{1}{v[(p_0/p)-1]} = \frac{c-1}{v_m c}\left(\frac{p_0}{p}\right) + \frac{1}{v_m c} \tag{3.1}$$

Where p and p_0 are the equilibrium and the saturation pressure of adsorbates at a constant temperature of adsorption. v and v_m are the total and monolayer adsorbed gas quantities. c is the BET constant. **Equation 3.1** is valid when plotted (known as a BET plot) as a straight line in the p/p_0 range of 0.05 to 0.35. As the monolayer volume is evaluated **Equation 3.2** and **Equation 3.3** can be used to determine the total analysed surface area (S_t) and the specific surface area (S_s).

$$S_t = \frac{v_m N s}{V} \tag{3.2}$$

$$S_s = \frac{S_t}{m} = \frac{v_m N s}{V m} \tag{3.3}$$

Here N is the Avogadro's number, s is the specific adsorption cross-section of the adsorbate, V is the molar volume of the adsorbate and m represents the mass of the analysed sample.

Experimental setup and process

A small filter sample was cut from the filter. Degassing is required prior to BET measurements for cleaning or removing the adsorbed gases on the surface. The sample was degassed in an oven at 90° C for 150 min. After degassing, the sample was inserted in the analysis cell and the experiment was conducted using nitrogen as the adsorbate gas.

3.2. Experimental Methodology for Chapter 5

3.2.1. Dynamic Vapor Sorption (DVS) of Grade 23 Ti6Al4V powders

DVS was used to quantify the vapour sorption properties for Grade 23 Ti6Al4V powders.

Instrumental operation principle

Please refer to Section 3.1.1. The DVS Intrinsic Plus (Sorption Measurement Systems, UK) used to characterize the Grade 23 Ti6Al4V powders.

Experimental setup and process

Dynamic vapour sorption (DVS) was conducted on as received Grade 23 Ti6Al4V powders (Tekna, Canada) using a DVS Intrinsic Plus (Surface Measurement Systems, UK). Approximately 100 mg powder was used for evaluating sorption isotherm loops from 0-80 % RH. The experiment was and repeated once as per the process detailed in Section 3.1.1 and **Figure 3.3**.

3.2.2. Morphology of Grade 23 Ti6Al4V powders

Powders used in LPBF AM are required to have spherical morphology with a smooth surface. It is also important to detect the presence of agglomerates or powders with satellite particles. Scanning electron microscopy (SEM) was used to image the powder morphology.

Instrumental operation principle

The Hitachi SU3500 (Hitachi, Japan) was used to characterize the Grade 23 Ti6Al4V powders. Please check Section 3.1.3. for details of its operating process.

Experimental setup and process

The Grade 23 Ti6Al4V powder sample was placed on carbon tape. This carbon tape was mounted on an aluminium holder and analysed using secondary electrons in the SEM. The experimental setup used a low pressure of 70 Pa, under 5 kV of accelerating voltage.

3.2.3. Particle Size Distribution of Grade 23 Ti6Al4V Powders

Particle size distribution (PSD) of Grade 23 Ti6Al4V powders were investigated. The PSD requires to be within specified limits required for usage in LPBF AM.

Instrumental operation principle

A laser scattering particle size distribution analyser Horiba LA-920 (Horiba, Japan) was employed to obtain the particle size distribution of the Grade 23 Ti6Al4V powders. Laser

scattering is based on the Fraunhofer criterion which states that the intensity of a laser scattering is directly proportional to the particle size. The angle of scattering is inversely proportional to the particle size as shown in **Figure 3.5**.

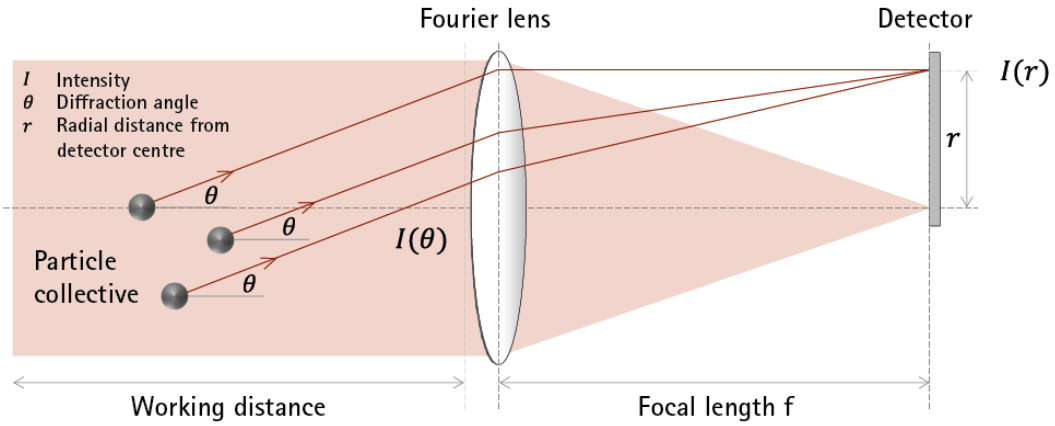

Figure 3.5. Schematic of laser scattering for powder size analysis [3.6].

The scattering angle is independent of the position or motion of the particles. A wide laser beam is directed on particles which are generally suspended within a fluid. The fluid can be a liquid (called 'wet' analysis) or a gas (called 'dry' analysis). A mechanical stirrer or a gas stream is usually available to keep the particles suspended in the 'wet' or 'dry' analysis respectively. The scattered angles and intensities are detected and correlated with the particle size using Fraunhofer's theory or in some instruments by using Mie's theory (A detailed description is available in these references [3.7,3.8]).

Experimental setup and process

1 g of Grade 23 Ti6Al4V powder was analysed using the Horiba LA-920 (Horiba, Japan) particle size distribution analyser. The 'wet' method of analysis was used as isopropanol was used to suspend the sample.

3.2.4. Surface Chemistry of Ti6Al4V powders

Analysis of the surface chemistry of Ti6Al4V powders indicates a presence, absence or extent of a chemical reaction on the powder surface. It is important to understand any chemical changes occurring due to storage or processing conditions on the powder. A depth profile of elemental composition change also provides further information on the powder surface chemistry change.

Instrumental operation principle

The surface chemistry of Ti6Al4V powders was characterized using x-ray Photoelectron Spectroscopy (XPS) [3.9]. In an XPS, a sample is placed in an evacuated chamber and a narrow-focused beam of X rays is projected upon the sample surface. Photoelectrons excited by the incident X rays are emitted from the near-surface region (top 0-20 nm). The kinetic energy and number of these photoelectrons are measured by a detector. The kinetic energy of the emitted photoelectrons can be related to the binding energy using **Equation 3.4**. Where E_b, E_p, E_k and ϕ are the binding energy, energy of the imparted X-ray photons, detected kinetic energy of the photoelectron and the work function respectively.

$$E_b = E_p - (E_k + \phi) \tag{3.2}$$

The binding energy of the electron provides the elemental band signature and the number of photoelectrons signifies the relative abundance of the element. Thus, the XPS is a robust method for the characterization of surface chemistry. Ion etching often using an argon sputter gun can be performed to reveal the chemistry of the underlying layers, this technique is known as XPS depth profiling.

Experimental setup and process

A Thermo Scientific K-Alpha (Thermo Scientific, USA) XPS system was used for the as-received Ti6Al4V and Ti6Al4V powders stored for 2 hours at 60 % RH in a controlled atmosphere glove box. Samples were initially degassed in vacuum for 1 hour to clean the surface. A small amount of the powder samples was fixed on carbon tape which was placed on an aluminium foil. The foil with the carbon tape was mounted on the sample mount and placed in the machine for analysis. The spot size was 400 um and the analysis was conducted in ultrahigh vacuum (at 9.38 x 10^{-8} Pa). To compare the surface oxides formed, the XPS elemental depth profile was captured using argon sputtering with an etching time of 250 s.

3.2.5. Specific Surface Area of Ti6Al4V Powders

Grade 23 Ti6Al4V powders are very fine allowing a higher specific surface area than coarser powders or bulk materials. Therefore, it is important to obtain a numeric value of the specific surface area.

Instrumental operation principle

Please refer to Section 3.1.4. The Micromeritics TriStar 3000 (Micromeritics Instrument Corporation, USA) gas sorption system was used to characterize the Grade 23 Ti6Al4V powders.

Experimental setup and process

Prior to BET testing, as-received Grade 23 Ti6Al4V powders were degassed in vacuum for 150 min at 240° C in an oven. Approximately 4 g of degassed powders was inserted in the analysis tube and the test was conducted using nitrogen was used as the adsorbate gas.

3.3. References

[3.1] Surface Measurement Systems. DVS Intrinsic Plus. Available at: https://www.surfacemeasurementsystems.com/products/dynamic-vapor-sorption-instruments/vapor-sorption-analyzer/dvs-intrinsic/. (Accessed: 2nd March 2020)

[3.2] Surface Measurement Systems. Dynamic Vapor Sorption. Available at: https://www.surfacemeasurementsystems.com/solutions/dynamic_vapor_sorption/.(Accessed: 2nd March 2020)

[3.3] Traceable. 4385 Traceable Memory Hygrometer/Thermometer. Available at: https://www.traceable.com/4385-traceable-memory-hygrometer-thermometer.html#product_tabs_description_tabbed. (Accessed: 2nd March 2020)

[3.4] Hitachi High-Technologies Global. Scanning Electron Microscope SU3500 : Available at: https://www.hitachi-hightech.com/global/product_detail/?pn=em-su3500. (Accessed: 2nd March 2020)

[3.5] Particle Analytical. BET (Brunauer, Emmett and Teller). Available at: https://particle.dk/methods-analytical-laboratory/surface-area-bet-2/.(Accessed: 2nd March 2020)

[3.6] Sympatec. HELOS. Available at: https://www.sympatec.com/en/particle-measurement/sensors/laser-diffraction/helos/.(Accessed: 2nd March 2020)

[3.7] Malvern Panalytical. Laser Diffraction Particle Size Analysis. Available at: https://www.malvernpanalytical.com/en/products/technology/light-scattering/laser-diffraction. (Accessed: 2nd March 2020)

[3.8] Anton Paar. Laser diffraction for particle sizing: Anton Paar Wiki. Available at: https://wiki.anton-paar.com/en/laser-diffraction-for-particle-sizing/.(Accessed: 2nd March 2020)

[3.9] Physical Electronics (PHI). X-Ray Photoelectron Spectroscopy (XPS) Surface Analysis Technique. Available at: https://www.phi.com/surface-analysis-techniques/xps-esca.html. (Accessed: 2nd March 2020)

Chapter 4

Contribution of cellulosic fibre filter on atmosphere moisture content in laser powder bed fusion additive manufacturing.

4.1. Preface

Chapter 4 is manuscript published in Scientific Reports (Nature Research, UK). The chapter focuses on filter papers as a potential source of moisture. Since filter papers are hydrophilic, a probability of moisture being retained and released within the system exists. This work provides the qualitative and quantitative role of moisture being absorbed by filters during storage and how can be released within the LPBF system. The citation information is provided as follows,

- Das, A., Muñiz-Lerma, J. A., Espiritu, E. R. L., Nommeots-Nomm, A., Waters, K., & Brochu, M. Contribution of cellulosic fibre filter on atmosphere moisture content in laser powder bed fusion additive manufacturing. *Scientific reports* **9**, 1-8 (2019).

Abstract

Cellulosic materials are commonly used to manufacture the particulate filters used in laser powder bed fusion (LPBF) additive manufacturing (AM) equipment. An experimental approach has been used to calculate the moisture quantity and kinetics of sorption in a cellulosic filter at varying relative humidity levels. A prediction of the amount of moisture which can be theoretically held within a filter during storage before its use has been

obtained. Subsequently, the quantity and the rate of moisture desorption which can be transferred into the build chamber during LPBF is presented. This work highlights the importance of filter storage and conditioning prior to use in additive manufacturing processing.

Keywords

Filters, Oxygen/Moisture, Composition, Additive manufacturing

4.2. Introduction

Powder bed fusion additive manufacturing is a layer-by-layer manufacturing technique that allows the fabrication of complex parts with enhanced functionality [4.1]. The successful adoption of AM technology has been fostered by improvements in powder feedstock quality and process optimization [4.2–5]. A key factor to be controlled in AM processing is the oxygen concentration within the build environment [4.6,4.7]. During laser powder bed fusion (LPBF) processing, oxygen concentration has been found to influence the composition of various alloys such as Ti-6Al-4V [4.8,4.9], Al-12 Si [4.10], IN 718 [4.11], 316 L SS [4.12] and 17 PH SS [4.12,4.13]. In some metallic systems like Ti-6Al-4V, the oxygen content even dictates the grade of the material (grade 23 vs grade 5), and ultimately the mechanical properties of the part [4.14,4.15].

The oxygen concentration variation in the built part can be affected by a variety of factors. It has been hypothesized that oxygen contributions can come from adsorbed moisture presents on the powder surface and in the filter, as well as inert gas quality contamination. Within this list, moisture, which is not always monitored, must be

controlled since its reaction with the melt pool and the surrounding high-temperature region can augment the oxygen contamination in the produced parts.

Metallic powders have been found to be one of the predominant sources which contribute moisture to the AM environment [4.3]. Work has shown that moisture can be adsorbed onto the powder surface through water-metal interactions and water-water hydrogen bonding [4.16]. The quantity of moisture adsorbed is alloy dependent, with surface roughness, the presence of oxide and surface impurity concentration all independently contributing [4.17]. Amongst other moisture sources, commercial 'high purity' argon gas, for example, has 3 ppm (by volume) of moisture contained within it [4.18]. This highlights the fact that even in a perfectly sealed AM unit, with dried AM powders, inherent moisture will still be present.

The filter is critical in the operation of the AM system, as it removes the airborne particles produced during the building process. An understanding of its behaviour within the build environment and its possible contribution of moisture to the machine atmosphere is required. Filters for AM are commonly fabricated using pleated cellulose paper [4.19,4.20] composed of wood fibres [4.21], which are formed from micro-fibrils of chainlike cellulose aggregates [4.22]. Cellulose has a semi-crystalline structure, it possesses an amorphous region with a high amount of available hydroxyl groups that have the potential to interact with moisture through hydrogen bonding [4.22,4.23]. In the presence of a certain amount of water vapour, a dynamic concurrent phenomenon of adsorption and desorption of the water molecules from the fibres continues until an equilibrium moisture content (EMC) is reached [4.24]. To date, no published literature is available assessing the contribution of moisture from filters in the LPBF AM environment.

Upon storage in an uncontrolled environment, filters can adsorb moisture from the atmosphere. LPBF AM operation is conducted in a controlled environment involving inert gases. During printer operation, the adsorbed moisture in the filter can potentially desorb leading to a reaction with the melt pool. This reaction can lead to an increase in oxygen content in the part and powders [4.25].

The presence of moisture in LPBF environment can lead to other issues too, research has shown that moisture present during processing has been linked with defects such as surface micropores and variations in density in parts produced by LPBF AM [4.10,4.26]. For this reason, Bourell *et al.* [4.27] recommended a thermal degassing pre-treatment prior to the laser processing of titanium powders to eliminate its effect; this highlighted the importance of moisture control in AM processing. For LPBF AM of titanium systems, it has been recommended to keep the cumulative oxygen and moisture content in the build chamber below one ppm [4.28].

The aim of the present work was to study the moisture sorption and desorption from an AM filter in order to quantify the possible moisture contribution during the printing process. Dynamic vapour sorption (DVS) analysis has been used to evaluate the sorption and desorption capability of an industrial AM filter to understand its behaviour during filter storage. Additionally, real-time moisture monitoring during chamber atmosphere preparation of an industrial AM unit was carried out. This contributes to filling the current knowledge gap present by identifying the filter as a source of moisture and assessing its contribution within the build chamber during processing in LPBF AM.

4.3. Materials and methods

The contribution of cellulosic fibre filter on the atmospheric moisture content in LPBF additive manufacturing was studied using E 1900L cellulosic filters sourced from Hengst SE, Germany, purchased from Renishaw Canada, Ltd. The filter was tubular in design, with a rubber top and base to hold concertinaed filter paper around the periphery, the filter dimensions were; 401 mm high, with an outer diameter of 195 mm and an internal hollow diameter of 118 mm.

Filters were characterised using variable pressure SEM imaging, using a Hitachi SU3500 Scanning Electron Microscope using a pressure of 70 Pa, under 10Kv. The specific surface area of the filter was measured via the Brunauer–Emmett–Teller (BET) method using a Micromeritics TriStar 3000 (Micromeritics Instrument Corporation, USA) gas sorption system.

The filters were received packaged in cardboard boxes with no internal wrapping. Throughout the study, the environmental RH measurements were carried out using a Traceable Memory Hygrometer (Fisher Scientific, USA). To determine the storage RH conditions of the filters, a set of measurements were taken inside the laboratory and from the inside of the cardboard storage container by inserting the hygrometer probe through 3 different filter storage containers.

The quantification of the moisture sorption and desorption capacity of the studied filter was carried out using the gravimetric dynamic vapour sorption (DVS) technique (DVS Intrinsic Plus, from Surface Measurement Systems, London, UK). The DVS Intrinsic apparatus measures mass change (±0.1 µg) under controlled temperature and humidity. Prior to testing, circular samples were punched from the filter using an APSCO

330A paper hole punch with a diameter of 6.35 mm (0.25 inch) and dried in an air atmosphere at 80 °C for 1 hr. Dried samples were loaded into an aluminium pan and placed into a chamber at a controlled temperature of 25 °C and allowed to reach equilibrium, i.e., until the change in mass as a function of time was less than 0.002% per minute. The sorption tests started by soaking the samples for 6 h in a flow of dry air to allow the chamber to reach 0 % relative humidity (RH). After 6 hrs of gas drying, the RH in the DVS chamber was increased in steps of 10% RH until 80% RH was reached. Each RH step was held until equilibrium. Once 80% RH was reached, the desorption test started by ramping down the RH from 80% to 0% in steps of 10% mirroring the ramp-up. To verify the DVS data for the moisture sorption capacity of the filters, three packaged filters stored under identical conditions were unpacked and consequently, oven-dried at 90 ^{o}C for five hours. The RH of storage within the laboratory for this case varied between 31 and 35 % over a period of 48 hours.

Once the adsorption and desorption capacity were measured via DVS, in situ measurements of RH during the chamber atmosphere preparation of a Renishaw AM250 with no powder were conducted. The RH variation as a function of time was recorded using a Fischer brand probe hygrometer installed in the build chamber. The LPBF machine used in the present study has the option to select between two different chamber atmosphere preparation methods. The first method denominated as *"with evacuation"*, consists of an evacuation step followed by a purging process. The evacuation step consists of extracting the gases present in the build chamber using a mechanical vacuum pump until a vacuum pressure of 40 mBar is reached. The purging process is carried out by filling the build chamber with Ar gas followed by the simultaneous injection and venting of Ar until the target oxygen concentration in the chamber was reached. The second chamber atmosphere preparation method denoted as *"without evacuation",* lacks an

evacuation step and only presents a purging process that is carried out until the target oxygen concentration was reached. In both methods, gas recirculation through the filter was periodically induced during the purging process. However, when the target concentration of oxygen was reached, gas recirculation was continuous until the printing process started.

In the present study, both methods, *"with evacuation"* and *"without evacuation"*, were used with a gas recirculation time of 5 minutes after 1000 ppm of oxygen concentration was reached. Three filter conditions were tested by both chamber atmosphere preparation methods for a total of six testing conditions as follows, in order to identify a baseline value of RH, the first pair of the tests consisted of the chamber atmosphere preparation methods were conducted without a filter. The second pair of tests were conducted using filters dried at 90 °C for 5 hr. Finally, the third pair of tests was performed using as-received filters stored under laboratory environment and denominated as 'non-dried filter'.

4.4. Results and Discussions

4.4.1. Filter Characterisation

Figure 4.1 shows the structural features of the filters surface, as shown the surface of the filter is made up of individual fibres forming a spaghetti-like structure ~ 20 µm in diameter; their surface roughness was typical for cellulosic materials. The surface area was measured via BET and was found to be 0.2491 m^2/g.

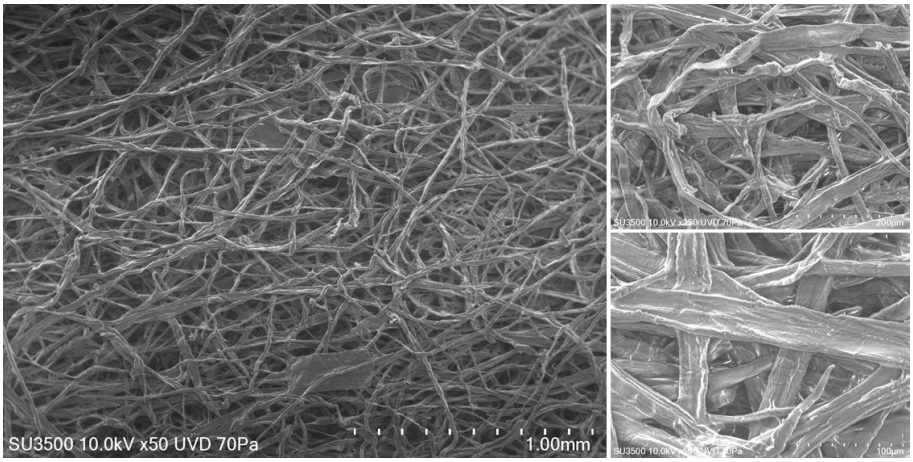

Figure 4.1. SEM images of the as-received filter surface at 50, 250 and 500x magnification.

4.4.2. Water vapour sorption and desorption characteristics

The DVS was utilised to determine the EMC of the filter as a function of the environmental RH. **Figure 4.2** (a) shows representative DVS sorption and desorption isotherm loops for two samples of filter paper. This data indicates that the sorption and desorption is a reversible process dependent on the subjected external RH. Hysteresis was observed as the EMC values are slightly higher upon desorption to the same RH level. As demonstrated, the reproducibility of the hysteresis was consistent. **Figure 4.2** (b) depicts the mass gain (during sorption) or mass loss (during desorption) for Sample 1. The blue coloured steps indicate the machine command (or target) stepwise increase/decrease in RH within the DVS chamber. Corresponding to this RH change, the red coloured steps indicates the change in mass of the specimen. It can be observed that this mass rise (on sorption) and mass loss (on desorption) was initially fast and stabilized by gradually

slowing down to reach the EMC value. For each of these steps in the DVS, stabilization to EMC required between 1-2 hours.

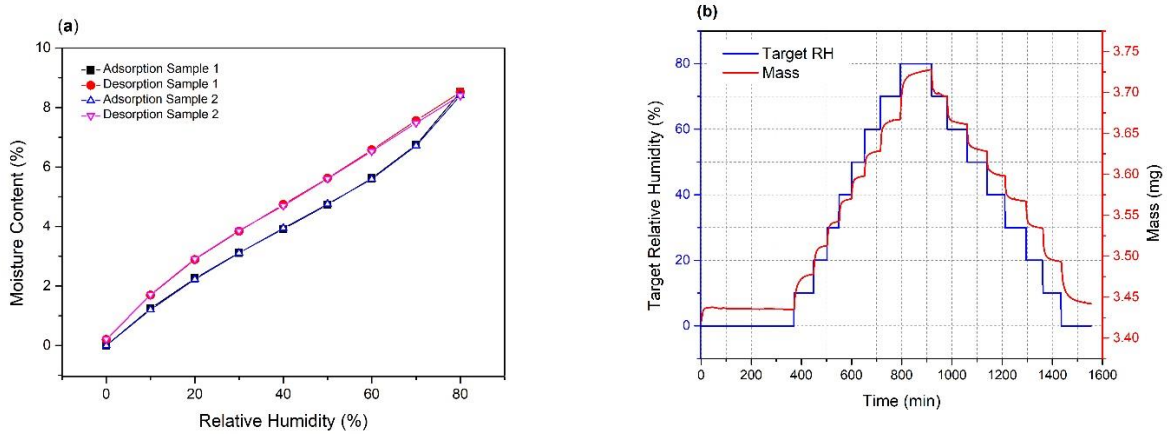

Figure 4.2. (a) DVS sorption/desorption isotherm loop for 2 samples, and (b) change in mass of sample 1 in response to the set RH values of the DVS sorption/desorption isotherm loop.

In order to explain the observed fast and slow mass change, a Parallel Exponential Kinetics (PEK) model was used to fit the data. In literature, this model was successfully used to model the DVS behaviour of various natural fibres including jute [4.21,4.22], coir [4.22], flax fibre [4.21,4.22], and hemp [4.21]. The PEK is based on a double exponential constituted of a fast and a slow step of moisture adsorption/desorption. Several mechanisms of moisture adsorption between the slow and fast processes have been proposed [4.29–32] but a coherent understanding of their physical meanings remains to be firmly established [4.21,4.24]. Hill et al. [4.24,4.33] postulate that the fast process in the PEK model represents adsorption or desorption of water molecules on readily available OH (hydroxyl) sites. The slow process in the PEK model has been associated with two possibilities, either to a gradual diffusion of moisture at less accessible sites within the

fibre or to swelling or shrinking of the fibre as sorption proceeds towards equilibrium [4.24].

Desorption within the machine may include a fast and a slow process constituting the exponential decay in the RH. This suggests a PEK type of model for data fitting. Interpretation of the PEK model fitting is complicated as the moisture allocation between the fast and slow processes is yet to be understood. For a better understanding of the physical process, a simple single exponential decay can be used because it is deemed sufficient to explain the initial fast and gradual slowdown phenomena as given in **Equation 4.1**,

$$\%RH = \%RH_{Stabilised} + C^{*}\exp(-t/t_1) \quad (4.1)$$

% RH refers to the RH within the chamber at time t, the equilibrium amount of moisture content within the chamber correspond to the % $RH_{Stabilised}$ value, C is a constant indicating the difference between the initial and stabilised RH and t_1 is the characteristic time (inverse of rate constant) which provides an indication of the length of time required for the RH content to stabilise.

4.4.2.1. Relating external storage RH to the packaged filter RH

The mean RH measured in the laboratory atmosphere and the filter storage box was 57.55 % (s = 0.45 %) and 56.11 % (s = 1.04 %) respectively. As indicated, a minor difference was observed. The similarity between the RH content outside and inside the storage box has been attributed to the permeability of the cardboard storage box [4.34]. Moreover, the cardboard boxes had openings due to folding at the corners that can facilitate air exchange with the local environment. Therefore, in the case of stored filters in cardboard boxes, the internal RH value can be assumed to be approximately equal to the RH value

outside of the box. In that context, the EMC within the filter is dependent upon the local RH in which the sample is stored, therefore, changes in geographical location and seasons will have significant effects on the moisture content present.

4.4.2.2. Quantity of moisture held in a filter during storage

In reality, filters might be stored for days or weeks before being used in a printer. During storage, they can accumulate moisture from their surroundings. DVS results have shown that it took 1-2 hours for the filter paper to reach EMC values for any RH increment/decrement step (**Figure 4.2** (b)), therefore it can be assumed that if filters are stored for several days they will reach their EMC values if ambient RH is constant. For complete oven drying at 90° C, the duration of five hours was found to be sufficient as the filter weight remained constant beyond five hours. Upon such drying conditions, three filters from long-term storage (31-35 % RH variation in past 48 hours) exhibited a mean moisture loss of 3.85 % with a low standard deviation of 0.28 % among the set. This shows each filter contained similar amounts of moisture compared to other filters stored under the same conditions. This moisture content is within or close to the EMC values corresponding to 31-35 % RH in the sorption isotherm loop obtained by the DVS (**Figure 4.2** (a)). Thus, during storage, the filter either sorbs or desorbs moisture to reach the EMC value corresponding to the external RH value. Therefore, the EMC values obtained using the DVS experiment can be multiplied by the dry weight of the filter to obtain the mass of stored moisture (scale-up).

Figure 4.3 provides this equilibrium scaled value of the mass of water stored within an actual filter at various RH values. To construct **Figure 4.3**, the mean dry weight of 606.35 g obtained by drying three filters was used for multiplication with the EMC values from the DVS sorption isotherm loop (**Figure 4.2** (a)). As demonstrated,

the EMC of the filter can vary significantly with storage humidity; i.e. the filter adsorbs a minimum of (values along adsorption line) 0-51.28 g of moisture corresponding to storage at 0-80 % RH.

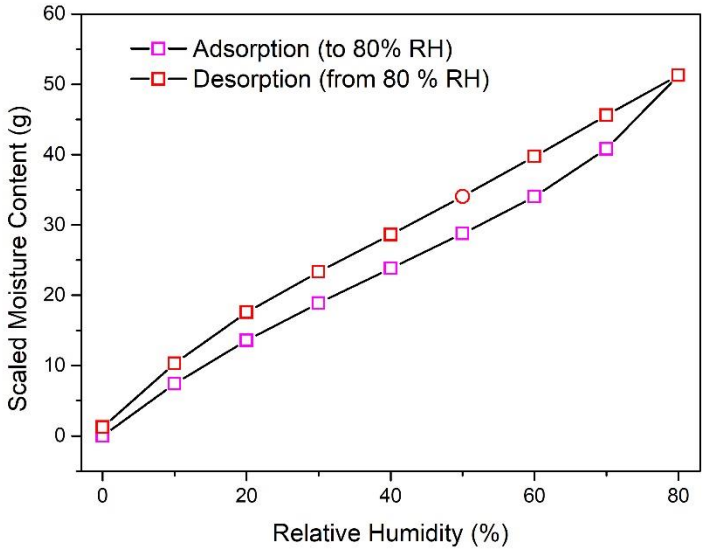

Figure 4.3. Scaled value of moisture content within a filter (mean dry weight 606.35 g) during sorption and desorption up to 80 % RH.

In the presence of a low RH environment, the adsorbed water on the filter can be desorbed. The chamber atmosphere preparation creates such a low RH environment within the build chamber either by evacuation or by purging dry inert gas it facilitates desorption. Therefore, during LPBF processing, the filter can act as an undesired source of moisture.

4.4.3. Moisture desorption from filters during chamber atmosphere preparation

4.4.3.1. For an LPBF AM build chamber with no filter unit

Figure 4.4 shows the change in measured RH during chamber atmosphere preparation with and without evacuation within the printing chamber when no filter unit is present. The initial chamber atmosphere preparation with or without evacuation follows an exponential decay pattern as represented by **Equation 4.1**.

As visualized in **Figure 4.4**, the experiment with evacuation initially had a faster decay rate which was around twice as fast when compared to the absence of evacuation. Additionally, the RH also stabilised quicker reflected by the lower characteristic time t_1 (0.44 min or 26.4 s compared to 1.05 min or 63 s). This shows that evacuation was more effective than purging gas and venting out moisture from the build chamber. Upon recirculation, RH values for both experiments remained stable at around 1-3 %. which is within the tolerance limit (4%) of the measuring hygrometer [4.35].

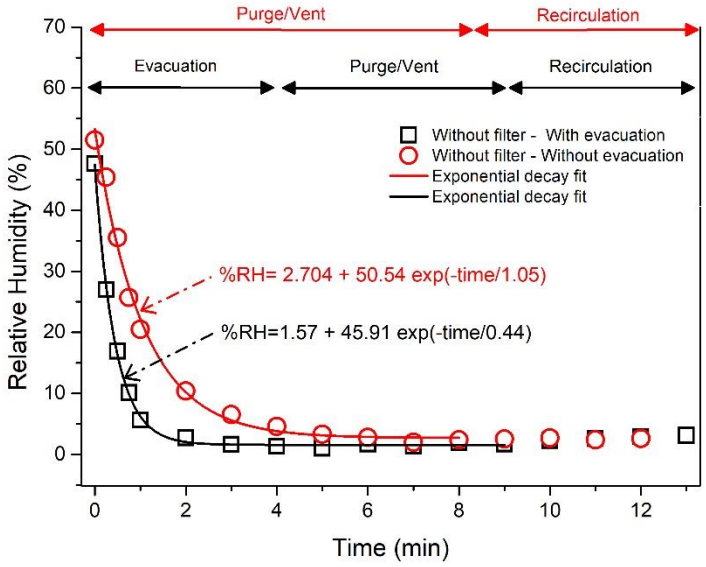

Figure 4.4. Variation of RH within the build chamber for the machine without a filter unit on a single purging/venting, recirculation cycle with evacuation and without evacuation.

4.4.3.2. For an LPBF AM build chamber with a dried filter unit

Figure 4.5 shows the relationship between RH and purge cycles conducted on an oven-dried filter. During the initial chamber atmosphere preparation with a dry filter, irrespective of the presence of evacuation, exponential decay in RH was observed with similar characteristic times as the experiment without the filter. Therefore, the removal of the moisture trapped in the chamber during either of the chamber atmosphere preparation was similar to the tests conducted with no filter unit (**Figure 4.4**). After 5 mins of recirculation, for both cases, the filters had low stabilised RH values which were preserved in contrast to those observed in the case of the experiments with the non-dry filter in Section 3.2.3.

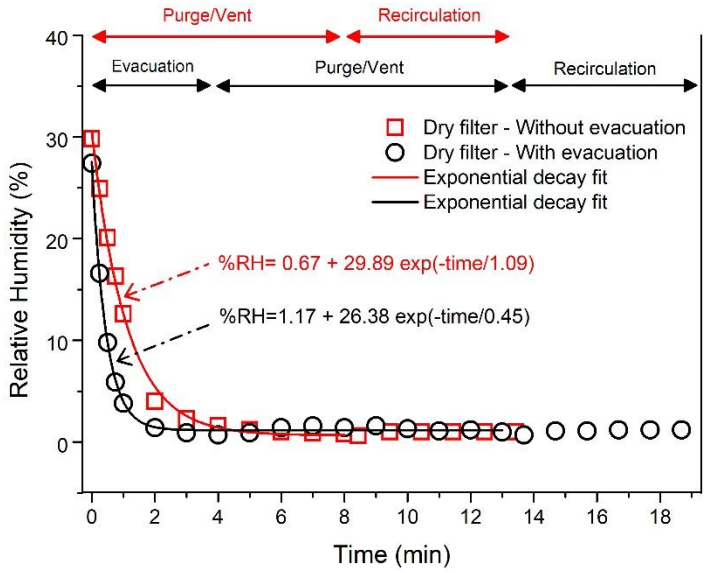

Figure 4.5. Variation of RH within the build chamber for the machine with a dried filter unit on a single purging/venting, recirculation cycle with evacuation and without evacuation.

4.4.3.3. For an LPBF AM build chamber with a non-dry filter unit

Figure 4.6 shows the change in RH with one printer chamber atmosphere preparation cycle with and without an evacuation cycle. In the initial stage, for both cases, the RH decays exponentially and can be described by **Equation 4.1**. The characteristic times for the experiment with evacuation is almost the same corresponding to the test without any filter and with a dried filter. This indicates a maximum value of chamber atmosphere moisture removal rate during the evacuation.

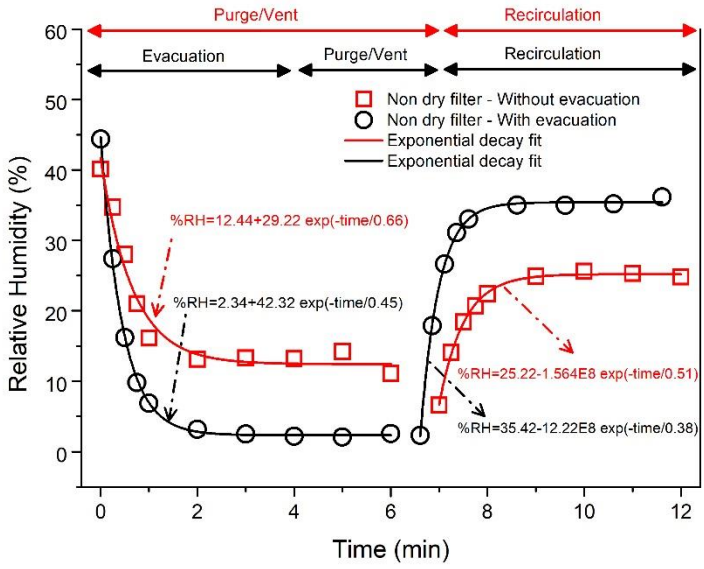

Figure 4.6. Variation of RH within the build chamber for the machine with a non-dry filter unit when subjected to a single purging/venting, recirculation cycle with evacuation and without evacuation.

The experiment without evacuation had two major purging and venting cycles. Therefore, the decrease in RH was in two steps, the initial first step and the second step beginning after 6 minutes. The observed initial RH drop was smaller when compared to the experiments without a filter and a dried filter. Thus, a shorter characteristic time was observed compared to the corresponding experiment without the filter and with a dried filter. Additionally, in the entire initial stage, it had a higher stabilized RH content compared to every other experiment; this points towards a supply of moisture from the non-dry filter during gas purging.

Upon recirculation of argon gas, the RH values in the chamber rose (**Figure 4.6**) and thereafter stabilised for both cases following an exponential decay pattern (**Equation 4.1**). The observed rise in RH occurs due to desorption of water molecules from the filter

interacting with the dry gas. The initial rapid gain of RH can be explained by a high rate of moisture release by the readily available desorption sites on the filter paper surface. The higher stabilised RH and shorter characteristic time for the experiment with evacuation indicate higher moisture content. The higher moisture content also readily translates into the presence of a higher number of available desorption sites which contributes to a faster desorption rate on recirculation. With time, gradually the contribution of desorption from the readily available desorption sites is reduced and desorption occurs from the lesser accessible sites. Thereafter, as the gas recirculated a steady equilibrium RH value was established within the machine.

For both experiments, the stabilised RH value after recirculation was lower compared to the initial RH, reflecting moisture loss from the filter. **Table 4.1** predicts an upper bound of the amount of moisture which could be reduced, utilizing the adsorption data from the scaled moisture content given in **Figure 4.3**. The RH value within the laboratory was the same as the initial RH measured in the experiment, as the LPBF system was open to the laboratory atmosphere prior to starting the experiment. In both experiments, the two filters have close initial RH values. Thus, they contained similar quantities (mass %) of moisture within them. Without evacuation or solely by purging/venting, this reduction of moisture content was greater than the experiment with the evacuation. The greater reduction can be attributed to the flowing inert gas within the system in case of purging which can interact with the filter causing faster desorption than in case of evacuation where the gas flow was absent.

Table 4.1. Prediction of moisture loss during initial chamber atmosphere preparation for a non-dry filter.

Experimental Process	RH value Initial (%)	RH value Stabilised (%)	Maximum Predicted Moisture Loss (g)
With evacuation	44.66	36.43	3.84
Without evacuation	41.64	25.27	7.68

4.5. Conclusion

This study utilises DVS and LPBF machine experiments to gain an understanding of how the filter cartridge can contribute to the moisture content in an LPBF AM system. Notable conclusions which can be drawn are;

1. Filters used in LPBF machines can adsorb moisture during storage unless sealed properly from the atmosphere or stored in zero RH environments. The amount of moisture adsorbed depends on the RH in which it was stored. The predicted amount of adsorbed moisture during storage ranged from 0-51.28 grams corresponding to 0-80 % environmental RH for a Hengst E1900 L air filter as shown in this study.

2. The filter loses some of its adsorbed moisture during both the chamber atmosphere preparation processes of evacuation and inert gas purging. The amount and rate of moisture loss are dependent upon the initial moisture stored in the filter and the parameters of the chamber atmosphere preparation processes. In this study, greater

desorption was observed in the case of inert gas purging compared to chamber evacuation from a non-dry filter.

3. Moisture in the LPBF chamber during processing can arise from the non-dry or a non-preconditioned filter unit. In the case of gas recirculation, the cyclic flow of inert gas established an RH equilibrium in the LPBF system.

4. Preconditioning the filter by drying for 5 hours at 90° C, successfully removed the entire moisture from the filter. An alternative strategy could be to store the filter in a place with low RH.

Although the exact contribution of the filter to the oxygen content will depend on a number of variables related to the specific LPBF equipment and the laser processing parameters, this study highlights the role of the filter in introducing moisture in the LPBF AM system. In absence of appropriate countermeasures, this can lead to an undesired increase of oxygen content in the expensive powders and parts.

4.6. References

[4.1] Campbell, I., Bourell, D. & Gibson, I. Additive manufacturing: rapid prototyping comes of age. *Rapid Prototyping Journal* **18**, 255–258 (2012).

[4.2] Berumen, S., Bechmann, F., Lindner, S., Kruth, J. P. & Craeghs, T. Quality control of laser- and powder bed-based Additive Manufacturing (AM) technologies. *Phys. Procedia* **5**, 617–622 (2010).

[4.3] Sames, W. J., List, F. A., Pannala, S., Dehoff, R. R. & Babu, S. S. The metallurgy and processing science of metal additive manufacturing. *Int. Mater. Rev.* **61**, 315–360 (2016).

[4.4] Ferrar, B., Mullen, L., Jones, E., Stamp, R. & Sutcliffe, C. J. Gas flow effects on selective laser melting (SLM) manufacturing performance. *J. Mater. Process. Technol.* **212**, 355–364 (2012).

[4.5] Dadbakhsh, S., Hao, L. & Sewell, N. Effect of selective laser melting layout on the quality of stainless-steel parts. *Rapid Prototyp. J.* **18**, 241–249 (2012).

[4.6] Gu Dongdong, W., Meiners, K. & Wissenbach, R. P. Laser additive manufacturing of metallic components: materials, processes, and mechanisms. *International Materials Review* **657**, 163–180 (2012).

[4.7] Murr, L. E. *et al.* Metal Fabrication by Additive Manufacturing Using Laser and Electron Beam Melting Technologies. *J. Mater. Sci. Technol.* **28**, 1–14 (2012).

[4.8] O'Leary, R., Setchi, R., Prickett, P., Hankins, G. & Jones, N. An Investigation into the Recycling of Ti-6Al-4V Powder Used Within SLM to Improve Sustainability. *SDM'2015 2nd Int. Conf. Sustain. Des. Manuf.* 14–17 (2015).

[4.9] Grainger, L. Investigating the effects of multiple powder re-use cycles In. *Addit. Manuf. Users Group; 28th Annu. Educ. Train. Conf.* 10–20 (2016).

[4.10] Li, X. P., O'Donnell, K. M. & Sercombe, T. B. Selective laser melting of Al-12Si alloy: Enhanced densification via powder drying. *Addit. Manuf.* **10**, 10–14 (2016).

[4.11] Ardila, L. C. *et al.* Effect of IN718 recycled powder reuse on properties of parts manufactured by means of Selective Laser Melting. *Phys. Procedia* **56**, 99–107 (2014).

[4.12] Barnhart, B. K. Characterization of Powder and the Effects of Powder Reuse in Selective Laser Melting. (Case Western Reserve University, 2017).

[4.13] Sun, Z., Tan, X., Tor, S. B. & Yeong, W. Y. Selective laser melting of stainless steel 316L with low porosity and high build rates. *Mater. Des.* **104**, 197–204 (2016).

[4.14] Yan, M. *et al.* Review of effect of oxygen on room temperature ductility of titanium and titanium alloys. *Powder Metall.* **57**, 251–257 (2014).

[4.15] Yan, M., Dargusch, M. S., Ebel, T. & Qian, M. A transmission electron microscopy and three-dimensional atom probe study of the oxygen-induced fine microstructural features in as-sintered Ti-6Al-4V and their impacts on ductility. *Acta Mater.* **68**, 196–206 (2014).

[4.16] Hodgson, A. & Haq, S. Water adsorption and the wetting of metal surfaces. *Surf. Sci. Rep.* **64**, 381–451 (2009).

[4.17] Kochsiek, M. Measurement of water adsorption layers on metal surfaces. *Metrologia* **18**, 153–159 (1982).

[4.18] Praxair Technology Inc. Argon Specification Sheet. Available at: https://www.praxair.com/-/media/corporate/praxairus/documents/specification-sheets-and-brochures/gases/argon/argon-ar-spec-sheet-ss-p4563.pdf. (Accessed: 23rd October 2018).

[4.19] Brown, G. W., Calcaterra, F. F. & Sleicher, D. Air filter element with radial sealing gasket. (1996).

[4.20] Davidson, T. *et al.* Apparatus and methods for handling materials in a 3-D printer. (2008).

[4.21] Xie, Y. *et al.* The dynamic water vapour sorption behaviour of natural fibres and kinetic analysis using the parallel exponential kinetics model. *J. Mater. Sci.* **46**, 479–489 (2011).

[4.22] Hill, C. A. S., Norton, A. & Newman, G. The water vapor sorption behavior of natural fibers. *J. Appl. Polym. Sci.* **112**, 1524–1537 (2009).

[4.23] Mokhothu, T. H. & John, M. J. Review on hygroscopic aging of cellulose fibres and their biocomposites. *Carbohydr. Polym.* **131**, 337–354 (2015).

[4.24] Hill, C. A. S., Norton, A. J. & Newman, G. The water vapour sorption properties of Sitka spruce determined using a dynamic vapour sorption apparatus. *Wood Sci. Technol.* **44**, 497–514 (2010).

[4.25] Saunders, S. R. J., Monteiro, M. & Rizzo, F. The oxidation behaviour of metals and alloys at high temperatures in atmospheres containing water vapour: A review. *Prog. Mater. Sci.* **53**, 775–837 (2008).

[4.26] Mukherjee, T., Zuback, J. S., De, A. & DebRoy, T. Printability of alloys for additive manufacturing. *Sci. Rep.* **6**, 1–8 (2016).

[4.27] Engel, B. & Bourell, D. L. Titanium alloy powder preparation for selective laser sintering. *Rapid Prototyp. J.* **6**, 97–106 (2000).

[4.28] Inert Corporation. Argon management for Additive Manufacturing. Available at: https://www.inerttechnology.com/systemapplications-overview/additive-manufacturing-solutions/argon-management/. (Accessed: 23rd October 2018).

[4.29] Kohler, R., Dück, R., Ausperger, B. & Alex, R. A numeric model for the kinetics of water vapor sorption on cellulosic reinforcement fibers. *Compos. Interfaces* **10**, 255–276 (2003).

[4.30] Okubayashi, S., Griesser, U. J. & Bechtold, T. A kinetic study of moisture sorption and desorption on lyocell fibers. *Carbohydr. Polym.* **58**, 293–299 (2004).

[4.31] Okubayashi, S., Griesser, U. J. & Bechtold, T. Water accessibilities of man-made cellulosic fibers - Effects of fiber characteristics. *Cellulose* **12**, 403–410 (2005).

[4.32] Kachrimanis, K., Noisternig, M. F., Griesser, U. J. & Malamataris, S. Dynamic moisture sorption and desorption of standard and silicified microcrystalline cellulose. *Eur. J. Pharm. Biopharm.* **64**, 307–315 (2006).

[4.33] Hill, C. A. S., Norton, A. & Newman, G. The water vapor sorption behavior of flax fibers - analysis using the parallel exponential kinetics model and determination of the activation energies of sorption. *J. Appl. Polym. Sci* (2010).

[4.34] Rasi, M. Permeability properties of paper materials (PhD thesis). (University of Jyväskylä, 2013).

[4.35] Fischer Scientific. Fisherbrand™ Traceable™ Memory Hygrometer/Thermometer. (2018). Available at: https://www.fishersci.ca/shop/products/c/06664271. (Accessed: 2nd November 2018)

Acknowledgements

The authors would like to thank the generous research support by the Natural Sciences and Engineering Research Council (NSERC) of Canada (NSERC Project Number: NETGP 494158 – 16 and Mitacs, Canada for providing support for one of the authors through the Globalink Graduate fellowship.

Author Contributions

A.D. and M.B. conceived the idea. A.D., J.A.M.L., A.N.N., and E.R.L.E. performed the experiments. A.D. analysed the data with consultation from every author. J.A.M.L, A.N.N., M.B., and K.W. contributed to a significant revision of the manuscript. All authors contributed to preparing the manuscript.

Additional Information

Competing interest statement: The authors declare no financial and non-financial competing interest.

Data availability statement: The experimental data presented in this paper is available for sharing upon request.

Chapter 5

Moisture adsorption on Ti6Al4V powders and the effect of storage in a humid environment.

5.1. Preface

This chapter is a manuscript focusing on the sorption behaviour of Ti6Al4V powders. Moisture can be also be hypothesized to originate from the adsorbed moisture on the powder surface. The previous chapter dealt with the quantification of moisture which can originate from the filter. In this chapter, moisture sorption and the effect of storage in a humid environment of commercial Ti6Al4V powder will be investigated. The manuscript is intended to be submitted for publication in 2019. The citation information is as follows:

- Das, E.R.L. Espiritu, K. Waters and M. Brochu*, "**Moisture sorption on Ti6Al4V powders and its effect of storage in a humid environment.**", *Article intended for publication, 2020.*

Abstract

Ti6Al4V powder feedstock used in LPBF AM is prone to oxygen contamination. The nature of water vapour (moisture) adsorption on the surface of a commercial feedstock Ti6Al4V powder has been studied using dynamic vapour sorption. The effect of humidity on the composition of these feedstock powders while in storage has also been studied. The

work aims to provide useful information storage and handling of feedstock Ti6Al4V powder.

5.2. Introduction

The properties of LPBF printed parts are directly affected by the quality of the feedstock powder. Moreover, the cost of the feedstock powders is also one of the major expenses in the overall LPBF process [5.1]. Therefore, maintenance of feedstock quality is necessary for LPBF AM.

Ti6Al4V parts are popularly used for biomedical implants [5.2] and aerospace structures [5.3]. Commercially two grades of Ti6Al4V powder corresponding to the oxygen content within the powders (Grade 5 – 0.2 % and Grade 23 – 0.13 %) are commonly used for LPBF AM. α Ti (HCP) has higher oxygen solubility since it has a large octahedral void and unfilled electron shells. It has the highest solubility for oxygen amongst all metals in the periodic table [5.4]. Consequently, Ti6A4V powders are susceptible to oxygen contamination. Thus, for Ti6Al4V powder, there lies a risk of oxygen contamination unless handled and processed properly.

Extensive literature detailing guidelines for powder storage and handling of Ti6Al4V was not identified. Nevertheless, certain important observations have been noted in the literature. Regarding storage, LPW technology conducted a study on storage of Grade 23 Ti6Al4V powders. It was found that the oxygen content on proper storage in sealed HDPE containers within an argon environment remained unchanged even after 9 years [5.5]. Titanium being reactive with oxygen, a natural coating of TiO_2 always exists on the powder surface. This oxide layer is protective in the absence of reactive conditions.

Therefore, on proper storage in argon, no adverse compositional uptake occurred in the case study by LPW technology.

Moisture has been known to be adsorbed on the powder surface of Ti6Al4V [5.6]. Porosity within parts [5.7] and poor flowability [5.8] have also been attributed to adsorbed moisture on the powder surface. At high temperatures such as in LPBF AM processing, a probability of moisture reaction exists. For these reasons, Engel [5.8] has recommended to oven-dry Ti6Al4V at 350 °C for degassing. The quantity of this adsorbed moisture and reactivity at room temperatures are unknown. This paper fills the knowledge gap by detailing the quantity of moisture which can be adsorbed by Ti6Al4V powder and whether storage in a moist environment for a short period of time affects the powder composition.

Although the current study focuses only on Ti6Al4V powders, there are other feedstock powders like AlSi10Mg which are also susceptible to oxygen contamination [5.9]. Additionally, there are a growing number of new feedstock material being developed for LPBF AM [5.10]. Proper storage, handling, and processing of these powders may also be required to maintain the quality of the produced parts. Therefore, further studies are required to fill the existing knowledge gap.

5.3. Materials and Methods

Plasma atomized Grade 23 Ti6Al4V powder feedstock used commercially for LPBF AM was obtained from Tekna (Tekna, Canada). The morphology of the powders was studied using a Hitachi SU 3500 scanning electron microscope. A Horiba LA-920 (Horiba, Japan) light scattering particle size distribution analyzer was used for obtaining the particle size distribution. The specific surface area of the powders was measured by a BET (Brunauer

Emmett Teller) method. A Micromeritics TriStar 3000 (Micromeritics Instrument Corporation, USA) gas sorption system was used for measuring the specific surface area of the powders. Nitrogen was used as the adsorbent gas.

Dynamic vapour sorption (DVS) was used to characterize the moisture sorption properties of the Ti6Al4V powders. A DVS intrinsic Plus (Surface Measurement Systems, UK) was used to obtain a sorption isotherm loop. The sorption tests started by exposing the samples for 6 hrs in a flow of dry air to allow the chamber to reach 0 % relative humidity (RH). After 6 hours of exposure to dry air, the RH in the DVS chamber was increased in steps of 10 % RH until 80 % RH was reached. Each RH step was held until equilibrium. Once 80 % RH was reached, the desorption test started by ramping down the RH from 80 % to 0 % in steps of 10 % mirroring the ramp-up. The experiments were repeated twice.

The as-received powder feedstock was stored within a standard powder cabinet (RH $<$ 2 %). To understand the effect of humidity on the composition, a portion of the 'as received' powders were stored for 2 hours in a glove box with an internal RH of 60 % (will be referred as the humid chamber). The period of 2 hours was selected to understand the effect of a 'short' exposure to water vapour (humidity). Its aimed to understand if a chemical change occurs if the powders are handled for short times before building in a room without humidity control. Immediately after storage, X-ray photoelectron spectroscopy using a Thermo Scientific K-Alpha (Thermo Scientific, USA) was conducted. An elemental depth profile corresponding to an argon sputtering time of 250 s was recorded. For comparison, an XPS depth profile was then conducted on the as-received powder. All experiments were conducted at room temperature.

5.4. Results and Discussions

Figure 5.1 (a) depicts powders used for LPBF AM. Due to plasma atomization, their morphology is spherical with low amounts of agglomeration. As these powders are highly spherical, they exhibit high flowability which is required for LPBF AM. **Figure 5.1** (b) shows the particle size distribution which mostly conforms to +20 -53 micron as specified by the manufacturer (Tekna). Thus, these powders possess the required characteristics to be used for LPBF AM.

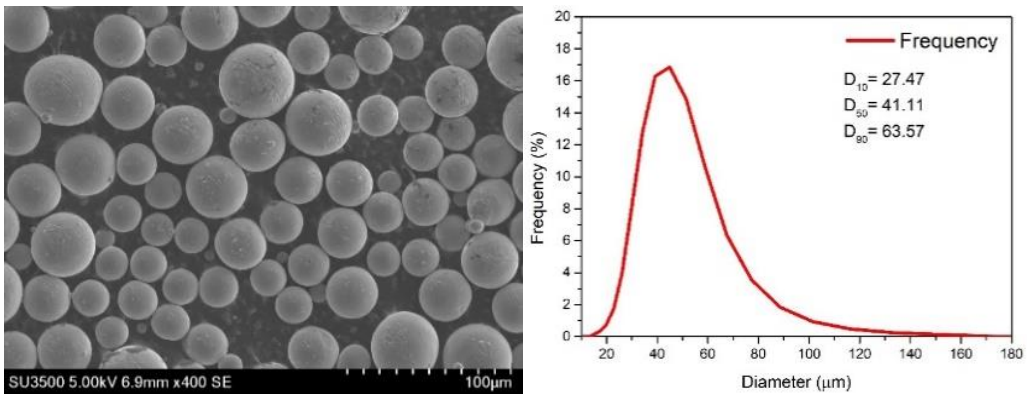

Figure 5.1. (a) SEM micrograph and (b) Particle size distribution of Grade 23 Ti6Al4V powders.

Figure 5.2 shows the sorption isotherm loop for Tekna Ti6Al4V powders. The maximum value of sorption recorded (~ 0.0035 % and 0.002 %) is above one order of magnitude of the detection limit of the instrument. The average specific surface area obtained from the BET experiments is 0.0411 m^2/g. Similar surface area values have for atomised Ti6Al4V powders is documented in the literature [5.8,5.11]. The smooth compact spherical morphology of the powder is responsible for this low value of the

specific surface area. Additionally, it also explains the low amounts of moisture sorption as the absence of pores leads to a lower amount of moisture sorption.

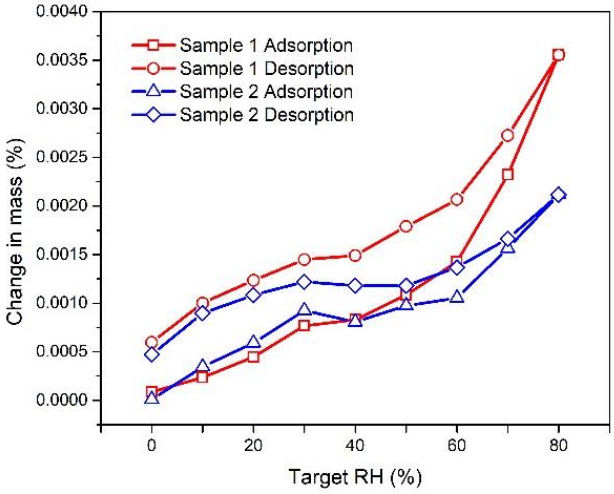

Figure 5.2. DVS sorption isotherm loop for two Grade 23 Ti6Al4V powder samples.

Figure 5.3 compares the XPS depth profile of the oxygen level of the sample stored at 60 % RH for 2 hours to the as-received sample. It can be observed that the oxygen content lowers with the sputtered depth in both cases. Only a small etch depth (in tens of Å) is possible within 250 s of argon sputtering. The oxygen depth profile of the sample stored in the humid chamber is only slightly above the profile of the as-received sample. This indicates that the oxygen composition change across the specimen is very similar for the stored sample.

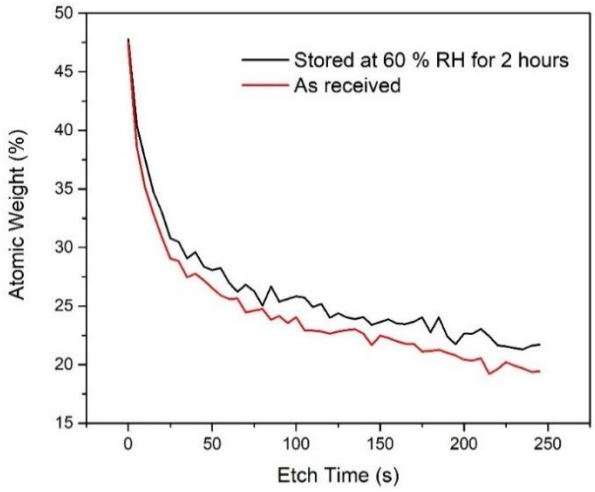

Figure 5.3. Comparison of the oxygen (O1s) depth profile of as received Ti6Al4V powder to the powder stored in a humid chamber.

The similarity of the depth profiles between the two samples shows the protective nature of the natural oxide scale (TiO_2). In this case, storage in moisture at room temperature did not have any adverse effect on the powder composition.

5.5. Conclusion

Moisture sorption for feedstock Ti6Al4V powders was analysed. At room temperature, it was found that the adsorbed amount of moisture is less than 0.005 % at high humidity values such as 80 % RH. The process is reversible i.e. desorption occurs on lowering the RH. XPS analysis of a powder sample stored in a humid chamber showed that no additional oxygen uptake is caused by storage of feedstock powders in a moist environment. Therefore, Ti6Al4V powder exposure or handling in a humid environment for short periods of time has less detrimental effects in terms of compositional changes.

5.6. References

[5.1] Medina, F. Reducing metal alloy powder costs for use in powder bed fusion additive manufacturing: Improving the economics for production. (The University of Texas at El Paso, 2013).

[5.2] Sing, S. L., An, J., Yeong, W. Y. & Wiria, F. E. Laser and electron-beam powder-bed additive manufacturing of metallic implants: A review on processes, materials and designs. *J. Orthop. Res.* **34**, 369–385 (2016).

[5.3] Liu, S. & Shin, Y. C. Additive manufacturing of Ti6Al4V alloy: A review. *Materials & Design* **164**, 107552 (2019).

[5.4] Kornilov, I. I. Effect of oxygen on titanium and its alloys. *Met Sci Heat Treat* **15**, 826–829 (1973).

[5.5] Additive Manufacturing UK. Case Studies. Available at: https://am-uk.org/case-studies/. (Accessed: 2nd March 2020)

[5.6] Haeussermann, H. M., & Joensson, S. Dynamic degassing of metal powders. *Progress in Powder Metallurgy* **41**, 25-34 (1985).

[5.7] Borofka, J. C., Tien, J. K. & Kissinger, R. D. Powder metallurgy and oxide dispersion processing of superalloys. *Superalloys, Supercomposites and Superceramics,* 237–284 (1989).

[5.8] Engel, B. & Bourell, D. L. Titanium alloy powder preparation for selective laser sintering. *Rapid Prototyping Journal* **6**, 97–106 (2000).

[5.9] Vock, S., Klöden, B., Kirchner, A., Weißgärber, T., & Kieback, B. Powders for powder bed fusion: a review. *Progress in Additive Manufacturing* **4**, 383–397 (2019).

[5.10] Niu, X. *et al.* Review of materials used in laser-aided additive manufacturing processes to produce metallic products. *Front. Mech. Eng.* **14**, 282–298 (2019).

[5.11] Munagala, V. N. V., Akinyi, V., Vo, P. & Chromik, R. R. Influence of Powder Morphology and Microstructure on the Cold Spray and Mechanical Properties of Ti6Al4V Coatings. *J Therm Spray Tech* **27**, 827–842 (2018).

Acknowledgements

The authors would like to thank the generous research support by the Natural Sciences and Engineering Research Council (NSERC) of Canada (NSERC Project Number: NETGP 494158 – 16 and Mitacs, Canada for providing support for one of the authors through the Globalink Graduate fellowship.

Author Contributions

M.B., A.D. and E.R.L.E. conceived the idea. A.D. and E.R.L.E. performed the experiments. K.W. helped in facilitating the experiments. A.D. and E.R.L.E. analysed the data with consultation from every author. A.D prepared the manuscript.

Additional Information

Competing interest statement: The authors declare no financial and non-financial competing interest.

Data availability statement: The experimental data presented in this paper is available for sharing upon request.

Chapter 6

Summary

Moisture is often an overlooked topic and has also been termed as an 'uncontrollable factor' in LPBF AM. This work aims to provide a better understanding of the origins of moisture in LPBF AM. An introduction to the thesis and a literature review detailing an overview of LPBF AM has been provided. The compositional issues in LPBF AM particularly detailing the powder requirements, factors affecting powder properties and effects in powder handling and recycling have been discussed. The final section of the literature review provides an overview of moisture sorption which is central to this thesis. All relevant experimental details have been provided in Chapter 3.

Two sources of moisture in LPBF AM were identified a) the cellulosic fibre filters used for LPBF AM and b) feedstock powders used in LPBF AM. The contribution of moisture from cellulosic fibre filters is discussed in Chapter 4. Cellulosic fibres are hydrophilic in nature, it was shown that these filters can adsorb a significant amount of moisture while being stored at an RH above zero. Upon usage in a low RH atmosphere such as LPBF AM, this adsorbed moisture on the filter was shown to be released. Preventive measures such as drying the filter prior to its use have been suggested to eliminate this problem. Chapter 5 presents a study of the sorption of moisture on powders for LPBF AM. Moisture sorption on a commercial Grade 23 Ti6Al4V powder was analysed using dynamic vapour sorption. Low quantities of moisture were found to be adsorbed on the powder surface. The effect of storage on the oxygen content of Ti6Al4V in a humid atmosphere at room temperature was studied. An XPS analysis with a depth

profile showed a negligible change in the oxide thickness. Therefore, in the case of Ti6Al4V, powders are not a significant source of moisture in an LPBF AM system.